

1 **Revision 2**

2 **Two discrete gold mineralization events recorded by hydrothermal xenotime and**
3 **monazite, Xiaoqinling gold district, central China**

4 Word Count: 10795

5 Wei Jian^{1*}, Jingwen Mao¹, Bernd Lehmann², Shitou Wu³, Lei Chen¹, Shiwei Song¹, Jiandong Xu^{1,4},
6 Peng Wang⁵, Junchen Liu¹

7 ¹ MNR Key Laboratory for Exploration Theory & Technology of Critical Mineral Resources, School
8 of Earth Sciences and Resources, China University of Geosciences (Beijing), Xueyuan Road 29,
9 Beijing, 100083, China

10 ² Mineral Resources, Technische Universität Clausthal, Adolph-Roemer-Strasse 2A, Clausthal-
11 Zellerfeld 38678, Germany

12 ³ State Key Laboratory of Lithospheric Evolution, Institute of Geology and Geophysics, Chinese
13 Academy of Sciences, Beitucheng Road 19, Beijing, 100029, China

14 ⁴ State Key Laboratory of Plateau Ecology and Agriculture, Qinghai University, Ningda Road 251,
15 Xining, 810016, China

16 ⁵ School of Earth Sciences and Spatial Information Engineering, Hunan University of Science and
17 Technology, Xiangtan 411201, China

18

19 *E-mail: weijian851@gmail.com

20

21

22

23

24

25

ABSTRACT

26 We present in situ LA-ICP-MS U-Pb dating of xenotime and monazite in assemblages with native
27 gold and Au (Ag) tellurides from the Xiaoqinling lode gold district in central China. Composite
28 xenotime and monazite grains formed through coupled dissolution–reprecipitation reactions reveal
29 two discrete gold mineralization events. The first gold mineralization event, recorded by monazite
30 (158.6 ± 3.3 Ma, Tera-Wasserburg lower intercept age) and xenotime cores (157.11 ± 0.83 Ma,
31 weighted mean $^{206}\text{Pb}/^{238}\text{U}$ age), is characterized by the mineral assemblage of lingbaoite (AgTe_3)-
32 sylvanite ($[\text{Au,Ag}]_2\text{Te}_4$)-stützite ($\text{Ag}_{5-x}\text{Te}_3$)/native tellurium-sylvanite-stützite. The second gold
33 mineralization event, recorded in the rims of xenotime (135.46 ± 0.93 Ma, weighted mean $^{206}\text{Pb}/^{238}\text{U}$
34 age), is characterized by the mineral assemblage of native gold-calaverite (AuTe_2)-petzite
35 (AuAg_3Te_2)-tellurobismuthite (Bi_2Te_3). Our study implies that the large-scale Jurassic mineralization
36 event in eastern China, related to flat subduction of the paleo–Pacific plate beneath the eastern China
37 continent, also caused widespread gold mineralization in the Qinling–Dabie Orogen, in addition to
38 production of its world-class porphyry Mo deposits. The fact that only a few Jurassic gold
39 mineralization ages have been reported before, may be due to the lack of suitable geochronometers to
40 record the earlier Jurassic hydrothermal processes, which have been overprinted by the better-
41 recognized Early Cretaceous gold mineralization event. This study also presents a rare example of
42 xenotime compositional alterations and resetting of U–Pb ages induced by low to moderate salinity
43 carbonic-aqueous fluids at low temperatures. The textural relationships between gold minerals in
44 contact with such composite xenotime crystals demonstrate that they could have precipitated before,
45 coeval with, or after the dated domains. Since low to moderate salinity carbonic-aqueous fluids are

2

46 commonly involved in the formation of lode gold deposits, it's crucial to examine xenotime textures
47 and recognize potential alteration textures before carrying out isotopic dating of xenotime collected
48 from these deposits. Without prior compositional and textural characterization, attempts to date such
49 composite crystals could yield mixed dates and meaningless ages.

50 **Keywords:** Xenotime, monazite, gold deposit, LA-ICP-MS U-Pb dating, Xiaoqinling, central China

51 INTRODUCTION

52 The formation of lode gold deposits commonly involves multiple hydrothermal stages or events
53 (e.g., Arne et al. 2001; Essarraj et al. 2001; Bateman and Hagemann, 2004; Meffre et al. 2016;
54 Fougereuse et al. 2017). The episodic nature of hydrothermal systems may be identified by well-
55 developed superimposed textures, such as breccias, ribbons, and a cross-cutting network of veinlets
56 (e.g., Dowling and Morrison, 1989; Goldfarb et al. 2005; Voisey et al. 2020; Jian et al. 2021).
57 However, it is challenging to determine whether vein systems result from the gradual cooling of a
58 single hydrothermal fluid or multiple hydrothermal events that occur millions of years apart. It is
59 especially difficult to accurately determine the timing of each individual hydrothermal event and the
60 timing of gold deposition. The difficulties mainly arise from the scarcity of suitable dating
61 minerals/mineral domains directly related to gold precipitation that remain closed to isotope re-
62 equilibration during subsequent hydrothermal events.

63 Monazite and xenotime are robust geochronometers that have low rates of Pb diffusion and low
64 susceptibility to Pb loss at high temperatures, with Pb closure temperatures of 890°C for xenotime
65 and 940°C for monazite (for a 10 µm grain with a cooling rate of 10°C/Ma: Cherniak et al. 2004;
66 Cherniak, 2006). However, the two minerals undergo coupled dissolution–reprecipitation reactions at

67 temperatures <400°C (Townsend et al. 2000; Rasmussen and Muhling, 2007; Budzyń et al. 2015a,b),
68 leading to crystals that may have multiple, but discrete, age domains from which precise dates for
69 multiple hydrothermal events may be obtained (e.g., Fielding et al. 2017; Budzyń et al. 2018).
70 Although many lode gold deposits contain trace amounts of hydrothermal monazite or xenotime, the
71 size of most hydrothermal xenotime grains is typically <10 µm, and combined with its low
72 abundance make it difficult to find suitable crystals from which complex, multi-stage hydrothermal
73 histories may be reconstructed (e.g., McNaughton and Rasmussen, 2018).

74 This study presents detailed in situ LA-ICP-MS U-Pb dating of xenotime and monazite in
75 assemblages with native gold and Au (Ag) tellurides from the Xiaoqinling lode gold district, central
76 China. Composite xenotime and monazite crystals formed through coupled dissolution–
77 reprecipitation reactions reveal two discrete gold mineralization events, with an early Cretaceous
78 gold mineralization event preceded by a previously overlooked middle Jurassic gold mineralization
79 event.

80 **GEOLOGICAL SETTING**

81 Marginal parts of the North China Craton host hundreds of lode gold deposits of mainly Early
82 Cretaceous age (Mao et al. 2005; Li et al. 2012a; Deng et al. 2016), with a total gold resource
83 exceeding 3,600 tonnes Au (Li et al. 2012a; Deng et al. 2016). The Xiaoqinling gold district in the
84 southern margin of the North China Craton represents the second-largest gold production area in
85 China, with a proven gold reserve of more than 630 tonnes (Jian et al. 2015, 2022a).

86 **Mesozoic tectonomagmatic evolution of the Qinling-Dabie orogen**

87 The Xiaoqinling district is located at the southern margin of the North China craton and belongs to
88 the Qinling-Dabie orogen (Fig. 1). The WNW-trending Qinling-Dabie orogen delineates the
89 boundary between the North China craton and the Yangtze craton. This orogenic belt resulted from
90 multistage collisional events between the North China craton and the Yangtze craton; the final
91 collision between the two cratons occurred in the Triassic (Dong and Santosh, 2016). During the Late
92 Triassic, the Qinling-Dabie orogen evolved into a post-collisional extensional domain, which is
93 indicated by the emplacement of post-collisional intrusions, including alkaline intrusions (Wang et
94 al. 2007; Li et al. 2012a; Cao et al. 2015), carbonatites (Xu et al. 2010; Du et al. 2020; Zheng et al.
95 2020; Tang et al. 2021), and rapakivi-textured granitoids (Wang et al. 2011).

96 Since the Jurassic, eastern China, including the eastern part of the Qinling-Dabie orogen, became a
97 part of the circum-Pacific tectonic regime, with the subduction of the Izanagi plate (or paleo-Pacific
98 plate) beneath the Eurasian continental margin (Mao et al. 2021a). The subduction began with a steep
99 angle but changed to a flat angle in the Middle-Late Jurassic (Wu et al. 2019; Mao et al. 2021a).
100 Since the Early Cretaceous, eastern China evolved into an extensional setting (Mao et al. 2021a) due
101 to lithospheric thinning driven by the rollback of the paleo-Pacific plate (Wu et al. 2019; Ma et al.
102 2021). The flat subduction and subsequent rollback of the paleo-Pacific plate gave rise to widespread
103 magmatism and ore formation, making the Late Mesozoic the most important magmatic and
104 metallogenic period in eastern China.

105 **Geology of the Xiaoqinling gold district**

106 The strata exposed in the Xiaoqinling gold district are dominated by Archean amphibolite-facies

107 metamorphic rocks of the Taihua Group (Fig. 1), which consists of biotite plagiogneiss, amphibolite
108 gneiss, amphibolite, quartzite, and marble (Cai and Su, 1985). These rocks probably formed in the
109 Neoproterozoic and have been subjected to amphibolite-facies metamorphism in the Paleoproterozoic
110 (Zhou et al. 1998; Ni et al. 2003; Li et al. 2007). The Archean rocks were intruded by
111 Paleoproterozoic pegmatite/granite (Li et al. 1996; Li et al. 2007), Proterozoic and Mesozoic granitic
112 intrusions (Wang et al. 2010; Hu et al. 2012; Li et al. 2012), and Paleoproterozoic and Early
113 Cretaceous mafic dikes (Wang et al. 2008; Bi et al. 2011). Jurassic magmatism, although widespread
114 in eastern China, has rarely been reported in the Xiaoqinling gold district. The Huashan granite
115 complex has a zircon age of 146 ± 2 Ma (Mao et al. 2010). Several Jurassic porphyritic stocks,
116 however, have been reported from the Xiong'ershan gold district, about 100 km east of the
117 Xiaoqinling district, and in a similar geologic setting (e.g., Niutougou, Miaoling, and Qiyugou gold
118 deposits: Wang et al. 2012; Li et al. 2014; Wang et al. 2020). However, these Jurassic porphyries do
119 not appear to be directly related to gold mineralization since they all postdate gold mineralization
120 (Wang et al. 2020). At the Qiyugou Au deposit, for instance, the quartz porphyries were emplaced at
121 158.6 ± 1.1 to 157.3 ± 1.1 Ma (LA-ICP-MS zircon U–Pb age), while gold mineralization occurred at
122 132.9 ± 1.5 Ma (molybdenite Re–Os age of gold ore samples) and is genetically related to the 130.9
123 ± 1.9 Ma hornblende monzogranite (LA-ICP-MS zircon U–Pb age).

124 Early Cretaceous plutons are widely exposed across the gold district. These are, from east to west,
125 the Niangniangshan biotite monzogranite (142 ± 3 to 129 ± 2 Ma: Wang et al. 2010; Li et al. 2012b),
126 the Wenyu biotite monzogranite (141 ± 2 to 136 ± 3 Ma: Wang et al. 2010; Li et al. 2012b), and the
127 outer phase of the Huashan granite complex (132 ± 1 Ma: Hu et al. 2012).

128 The nearly E–W–striking Taiyao and Xiaohe faults define the northern and southern boundaries of

129 the Xiaoqinling gold district. The two normal faults developed during the Cenozoic extension,
130 resulting in the exposure of the basement rocks (Li et al. 2020). The more than 1,200 gold-bearing
131 quartz veins concentrate along the axes of several EW-striking steep folds and are controlled by
132 small- to medium-size EW-striking faults. The S16 gold-bearing quartz vein, from which the studied
133 ore samples were collocated, is about 30 km southwest of Lingbao city, Henan province, central
134 China. The S16 gold-bearing quartz vein, from which the studied ore samples were collocated, is a
135 newly discovered concealed vein with an average gold grade of ~6 g/t. It is 0.1 to 2.5 m wide and
136 extends about 1.5 km in a roughly east-west direction, dipping to the south (Fig. 1). The S16 gold-
137 bearing quartz vein is about 30 km southwest of Lingbao city, Henan province, central China, and
138 belongs to the south ore belt of the Xiaoqinling gold district. The south ore belt hosts most of the
139 gold-bearing quartz veins, which concentrate along the Laoyacha anticline (Fig. 1).

140

SAMPLE MATERIAL AND METHODS

141 **Sample selection**

142 The studied ore samples were collected underground from the S16 gold-bearing quartz vein. The
143 ore samples for geochronological study consist mainly of quartz and pyrite (Fig. 2). Other minerals
144 present in small or trace amounts include xenotime, monazite, scheelite, celestine, gold, native
145 tellurium, muscovite, as well as a variety of sulfides (e.g., chalcopyrite, bornite, sphalerite, and
146 galena) and tellurides (e.g., sylvanite, petzite, calaverite, stützite, hessite, altaite, rucklidgeite, and
147 tellurobismuthite).

148 **Analytical methods**

149 Xenotime and monazite in polished thick sections were first examined in reflected light and then
150 by electron probe microanalysis (EPMA) and scanning electron microscopy (SEM). SEM
151 investigation was carried out at the Institute of Geology, Chinese Academy of Geological Sciences,
152 using a FEI NOVA nanoSEM equipped with an Oxford X-Max 50 detector. EPMA wavelength-
153 dispersive X-ray spectrometry (WDS) analysis was carried out at the Institute of Mineral Resources,
154 Chinese Academy of Geological Sciences, using a JXA-iHP200F electron microprobe. Details on
155 EPMA settings for WDS analysis are available in Table A1. EPMA X-ray mapping was carried out at
156 the State Key Laboratory of Plateau Ecology and Agriculture, Qinghai University, China, using a
157 JXA-8230 electron microprobe.

158 LA-ICP-MS U–Th–Pb isotope analysis of xenotime and monazite, as well as LA-ICP-MS trace
159 element analysis of xenotime, were carried out at the State Key Laboratory of Lithospheric
160 Evolution, Institute of Geology and Geophysics, Chinese Academy of Sciences. Analytical procedure
161 for U–Th–Pb isotope analysis follows Wu et al. (2020). Analytical details are available in Tables A2,
162 A3. LA-ICP-MS trace element analysis of monazite was carried out at the Yanduzhongshi
163 Geological Analysis Laboratories Ltd., Beijing, using a New Wave NWR 193 laser ablation system
164 coupled to an Analytikjena M90 quadrupole ICP-MS. Analytical details are available in Table A4.

165 **RESULTS**

166 **Vein mineralogy and paragenesis**

167 At least three hydrothermal stages, including two gold-mineralization stages, are recognized in the

168 studied ore samples (Figs. 2, 3, 4). The first hydrothermal stage (I) is characterized by the
169 precipitation of milky white quartz, which makes up more than 90% of the vein volume. The second
170 stage (II) is characterized by the growth of pyrite, scheelite, xenotime, monazite, and celestine on
171 fracture planes in quartz (Fig. 2). Pyrite contains composite mineral inclusions (<1–50 μm in
172 diameter) consisting mainly of lingbaoite (a recently named mineral with the chemical formula of
173 AgTe_3 , Jian et al. 2020), sylvanite $[(\text{Au},\text{Ag})_2\text{Te}_4]$, stützite $[\text{Ag}_{5-x}\text{Te}_3]$, native tellurium, and
174 chalcopyrite, with minor bornite, galena, and altaite (Figs. 3A–G). These inclusions outline the
175 primary growth zones in pyrite and generally display a negative crystal shape. They were interpreted
176 as primary melt inclusions, which were trapped as polymetallic melt droplets during the growth of
177 the host pyrite (Jian et al. 2021, 2022b). The third stage (III) is the main gold deposition stage. This
178 stage is characterized by native gold and tellurides (petzite $[\text{AuAg}_3\text{Te}_2]$, calaverite $[\text{AuTe}_2]$,
179 tellurobismuthite $[\text{Bi}_2\text{Te}_3]$, altaite $[\text{PbTe}]$, and rucklidgeite $[\text{PbBi}_2\text{Te}_4]$) as inclusions or fracture
180 fillings in early minerals (e.g., quartz, pyrite, and scheelite, Figs. 2–4). The stage III gold-bearing
181 mineral assemblages (e.g., native gold-calaverite-petzite-tellurobismuthite) commonly coexist with
182 low to moderate salinity $\text{H}_2\text{O}-\text{CO}_2$ fluid inclusions along healed fractures in quartz (Figs. 3I–K). The
183 total homogenization temperatures of these fluid inclusions have been investigated from many gold-
184 quartz veins in the Xiaoqinling gold district and cluster at 200 to 400°C (Fan et al. 2003; Li et al.
185 2012b; Xiong et al. 2013). The cross-cutting relation between stage II and stage III gold-bearing
186 minerals is illustrated in Figures 3A–B, in which stage II tellurides occur as inclusions in pyrite
187 while stage III gold and tellurobismuthite occur along quartz grain boundaries.

188 **Characterization of xenotime and monazite**

189 Xenotime and monazite crystals occur as inclusions in pyrite and scheelite, or along quartz
190 fractures (Figs. 2D, 4). Individual xenotime and monazite crystals are typically 10–80 μm in
191 diameter (Figs. 4–6), but large crystals (up to 350 μm in diameter, Figs. 4H, I) have also been
192 observed. The two minerals most commonly occur in contact with each other, and monazite has also
193 been observed as inclusions in xenotime. Cathodoluminescence (CL) imaging of xenotime reveals
194 that xenotime crystals have a dark, pristine core surrounded by bright altered domains, which
195 developed near grain rims or healed microfractures (Figs. 4I, 5). There is a sharp reaction front
196 between altered and pristine xenotime domains (Figs. 4D–I, 5). The xenotime cores display distinct
197 oscillatory zoning truncated at the boundary with the altered domains (Fig. 5). There is an epistatic
198 relationship between altered and pristine xenotime domains. For example, examination of the
199 xenotime crystals using polarized light shows that altered and pristine xenotime domains in each
200 grain are optically continuous (Figs. 4D, F, H). Altered xenotime also preserves the external
201 dimension of pristine xenotime. These textural features suggest that the altered xenotime domains in
202 our sample set formed through coupled dissolution-reprecipitation reactions (e.g., Putnis, 2002,
203 2009). Native gold and stage III tellurides have been observed as inclusions in the altered domains of
204 xenotime, or occur in contact with the altered domains (Figs. 4D–I).

205 Xenotime cores and rims show distinct major and trace element features (Tables A5, 6, Fig. A2).
206 EPMA analysis shows cores contain higher and more consistent Y concentrations (0.91–0.92 apfu,
207 atoms per formula unit on the basis of 4 oxygens) whereas Y concentrations in the altered rims vary
208 from 0.81 to 0.92 apfu. LA-ICP-MS trace element analysis reveals xenotime cores contain 1.4–4.1
209 wt% LREE (La to Eu), 9.0–13.0 wt% HREE (Gd to Lu), 1000–2600 ppm Si, 730–4600 ppm Ca,

210 12–19 ppm Rb, 5–19 ppm Sr, 29–220 ppm Zr, 240–620 ppm Pb, 1000–5800 ppm Th, and 1900–
211 5900 ppm U, while xenotime rims have higher concentrations of HREE (12.4–19.5 wt%), Si (0.1–2.1
212 wt%), and Rb (25–37 ppm), and lower concentrations of LREE (0.7–1.2 wt%), Zr (10–106 ppm), Pb
213 (84–256 ppm), Th (500–1900 ppm), and U (800–2400 ppm). In the chondrite-normalized REE
214 pattern (Fig. 7), neither the cores nor rims have an Eu anomaly. This differs from igneous xenotime,
215 which is commonly characterized by a pronounced negative Eu anomaly (e.g., Rasmussen, 2005;
216 Aleinikoff et al. 2015).

217 While xenotime crystals may show well-formed crystal faces, monazite occurs as subhedral-
218 anhedral grains, which form larger aggregates with irregular outlines (Fig. 6). Occasionally, elongate
219 monazite grains grow as radial, flower-shaped assemblages (Figs. 6, A3). Monazite shows a faint
220 core-rim texture under high-contrast SEM-BSE imaging (Fig. 6). The core has a heterogeneous
221 texture with chaotic, patchy zoning, and contains a dense population of mineral inclusions (≤ 10 μm ,
222 mainly iron oxides) and smaller fluid inclusions. The rim is relatively homogenous and inclusion-
223 free, with faint patchy zoning. Like xenotime, the monazite rim may preserve the external dimension
224 of pristine monazite (e.g., the top right monazite grain in Fig. 6), suggesting the altered rim formed
225 through coupled dissolution-reprecipitation reactions. The heterogeneous core represents a mixture
226 of pristine and secondary monazite.

227 EPMA WDS analysis (Table A5) and X-ray mapping reveal that monazite rims contain 0.01–0.08
228 apfu Si, 0.007–0.014 apfu Th, 0.23–0.26 apfu La, 0.41–0.45 apfu Ce, 0.09–0.12 apfu Pr, and 0.12–
229 0.15 apfu Nd, while the partially altered cores have lower concentrations of Si (0.01–0.06 apfu), Th
230 (0.005–0.007 apfu), and La (0.21–0.23 apfu), and higher concentrations of Nd (0.15–0.16 apfu).
231 Other elements show little systematic variation between the core and rim. LA-ICP-MS trace element

232 data of monazite are available in Table A7. LA-ICP-MS analysis (a spot size of 10 μm) does not have
233 the spatial resolution to resolve the altered monazite rim and the partially altered monazite core.
234 Monazite shows an LREE-enriched smooth pattern in the chondrite-normalized REE diagram,
235 without a distinct Eu anomaly (Fig. 7).

236 **U-Th-Pb isotope data**

237 One hundred and thirteen U–Th–Pb isotopic analyses were carried out on ten xenotime crystals.
238 The locations of analyses, along with the analytical numbers and apparent $^{206}\text{Pb}/^{238}\text{U}$ ages, are
239 presented in Figure 5. U–Th–Pb isotope data are listed in Tables A8 and presented graphically in
240 Figure 9. Among them, 33 analyses are not considered geologically significant and are excluded
241 from the age analysis. The omitted analyses include 20 analyses with discordance values ($1 -$
242 $^{206}\text{Pb}/^{238}\text{U}/^{207}\text{Pb}/^{235}\text{U}) \times 100) >5\%$ or $<-5\%$ and 13 analyses obtained from the incompletely altered
243 domains of xenotime. Explanations for the discordance and incompletely altered domains are
244 presented in the “Discussion” section.

245 After exclusion of the omitted analyses, the 46 analyses of pristine xenotime cores yield $^{206}\text{Pb}/^{238}\text{U}$
246 dates from 164.4 ± 6.1 to 153.2 ± 5.6 Ma, $^{207}\text{Pb}/^{235}\text{U}$ dates from 160.6 ± 6.9 to 152.2 ± 6.0 Ma, and
247 $^{208}\text{Pb}/^{232}\text{Th}$ dates from 168.2 ± 11 to 139.1 ± 7.6 Ma. These data define a weighted mean $^{206}\text{Pb}/^{238}\text{U}$
248 age of 157.11 ± 0.83 Ma (MSWD = 0.71), a weighted mean $^{207}\text{Pb}/^{235}\text{U}$ age of 155.93 ± 0.93 Ma
249 (MSWD = 0.60), and a Tera-Wasserburg lower intercept age of 156.49 ± 0.94 Ma (MSWD = 0.55).
250 The three ages overlap with each other within the margin of error. The remaining 41 analyses of
251 xenotime rims yield $^{206}\text{Pb}/^{238}\text{U}$ dates from 142.4 ± 5.8 to 128.5 ± 5.1 Ma, $^{207}\text{Pb}/^{235}\text{U}$ dates from 146.9
252 ± 9.4 to 129.4 ± 7.2 Ma, and $^{208}\text{Pb}/^{232}\text{Th}$ dates from 150.0 ± 21 to 121.5 ± 9.1 Ma. These data define

253 a weighted mean $^{206}\text{Pb}/^{238}\text{U}$ age of 135.46 ± 0.93 Ma (MSWD = 1.07), a weighted mean $^{207}\text{Pb}/^{235}\text{U}$
254 age of 135.2 ± 1.4 Ma (MSWD = 1.05), a Tera-Wasserburg lower intercept age of 135.5 ± 1.1 Ma
255 (MSWD = 1.05), and a Concordia age of 135.33 ± 0.91 Ma (MSWD = 0.41). The four ages overlap
256 with each other within the margin of error.

257 Thirty-eight U–Th–Pb isotopic analyses were collected on 11 monazite crystals. The locations of
258 analyses and analytical numbers, along with the apparent $^{206}\text{Pb}/^{238}\text{U}$ ages, $^{207}\text{Pb}/^{235}\text{U}$ ages, and
259 $^{208}\text{Pb}/^{232}\text{Th}$ ages, are shown in Figure 6. Results are listed in Table A9 and presented graphically in
260 Tera-Wasserburg Concordia diagram in Figure 8. Monazite shows large variations in $^{207}\text{Pb}/^{235}\text{U}$
261 (3730 ± 36 to 208 ± 8 Ma), $^{206}\text{Pb}/^{238}\text{U}$ (1897 ± 61 to 161 ± 6 Ma), and $^{208}\text{Pb}/^{232}\text{Th}$ dates (463 ± 15 to
262 141 ± 5 Ma). The U–Pb ages are highly discordant, with discordance values ranging from 23 to 79.
263 Nevertheless, the U–Pb isotope dataset forms a linear array in the Tera-Wasserburg Concordia
264 diagram, yielding an upper intercept age of >4.5 Ga and a lower intercept age of 158.6 ± 3.3 Ma
265 (MSWD = 3.7), which overlaps with the ages of xenotime cores within the margin of analytical error.

266

DISCUSSION

267 **Remarks on monazite and xenotime ages**

268 Although many monazite and xenotime dates are concordant or near concordant, the two minerals
269 may be affected by low-temperature hydrothermal alteration and yield discordant ages (e.g.,
270 Rasmussen et al. 2011; Seydoux-Guillaume et al. 2012; Didier et al. 2013; Budzyń et al. 2018, 2021,
271 2022; Budzyń and Sláma, 2019). Factors causing age discordance during hydrothermal alteration
272 include incomplete replacement of mineral domains (Grand'Homme et al. 2016; 2018) and

273 incorporation of initial Pb in secondary monazite and xenotime (e.g., Seydoux-Guillaume et al. 2012;
274 Didier et al. 2013; Budzyń et al. 2022). For instance, altered monazite domains with apparently
275 homogeneous composition at a microscale may correspond to nanomixtures of primary and
276 secondary monazite, yielding discordant ages (Grand'Homme et al. 2016; 2018). During
277 hydrothermal alteration of monazite, initial Pb could accumulate in the monazite lattice along the
278 microcracks (e.g., Budzyń et al. 2022) or be incorporated as nanosized Pb-rich inclusions (Seydoux-
279 Guillaume et al. 2003; Fougereuse et al. 2018).

280 Twenty analyses of xenotime yield highly discordant dates with >5% or <-5% discordance,
281 suggesting the incorporation of common Pb. Among them, thirteen analyses were obtained from the
282 rims, two from the cores, and three from the incompletely altered domains. Eleven analyses
283 with >5% discordance were placed on micro-fracture or porous places (e.g., analytical points 1 and 7
284 in section V16-101A, see the top left xenotime grain in Figs. 5, A1). Common Pb could present as
285 nano-scale Pb-bearing minerals, such as altaite (Pb as an essential element) or tellurobismuthite (Pb
286 as a minor component), along monazite microcracks and grain boundaries. Two minerals are
287 commonly observed to occur in contact with xenotime and monazite (Fig. 4C). Accordingly, we
288 propose the source of common Pb can be attributed to micro-cracks or porous spaces, which are
289 more developed in xenotime rims. Quartz is another source of common Pb. Eight analyses designed
290 to analyze the thin xenotime rims are contaminated by the quartz matrix; it is visible from the laser
291 ablation pits that quartz was ablated (e.g., analytical points 19–21 in section V16-103A, see the
292 central right xenotime grain in Figs. 5, A1). Common Pb could be present within quartz-hosted fluid
293 inclusions or along the grain boundaries between quartz and xenotime. Thirteen analyses obtained
294 from the incompletely altered domains (i.e., mixture of pristine and secondary xenotime) of xenotime

295 are also excluded from the age analysis. In Figure 5 (section V16-103A, the large grain in the top
296 right) and Figure A2 (xenotime in the third row), for instance, the incompletely altered domain in the
297 upper part of a xenotime grain partially preserves the oscillatory zoning of the pristine xenotime
298 core. Ages and U-Th concentrations of this domain fall between the pristine core and the completely
299 altered rim on the left.

300 Monazite shows highly discordant U-Pb ages (discordance values ranging from 23 to 79) and
301 large variations in $^{207}\text{Pb}/^{235}\text{U}$ (3730–208 Ma), $^{206}\text{Pb}/^{238}\text{U}$ (1897–161 Ma), and $^{208}\text{Pb}/^{232}\text{Th}$ ages (463–
302 141 Ma). Nevertheless, the U-Pb isotope dataset forms a linear array in the Tera-Wasserburg
303 Concordia diagram, with an upper intercept age of >4.5 Ga and a lower intercept age of 158.6 ± 3.3
304 Ma (MSWD = 3.7), suggesting the discordance is caused by the incorporation of common Pb (e.g.,
305 Schoene, 2004), which affected the more sensitive $^{207}\text{Pb}/^{235}\text{U}$ ratio (e.g., Budzyń et al. 2022).

306 The source of common Pb may be attributed to the extensive micro-cracks and grain boundaries,
307 which are not easily recognized under the optical microscope but become apparent under high-
308 contrast SEM-BSE imaging. Analytical spots placed within individual monazite grains without
309 visible micro-cracks (e.g., analytical spots 15–21 in section V16-103a, Fig. 6) show younger
310 $^{207}\text{Pb}/^{235}\text{U}$ and $^{206}\text{Pb}/^{238}\text{U}$ ages than those placed in monazite aggregates with grain boundaries and
311 micro-cracks (e.g., analytical spots 1–14 in section V16-103a, Fig. 6). Common Pb could accumulate
312 in the monazite lattice along the microcracks (e.g., Budzyń et al. 2022). Similar to xenotime,
313 common Pb could also present as nano-scale Pb-bearing minerals, such as altaite or
314 tellurobismuthite, along monazite microcracks and grain boundaries. The abundant mineral
315 inclusions in monazite are less likely to be the sources for common Pb, because X-ray mapping shows
316 that the inclusions contain lower Pb concentrations than the surrounding monazite (Fig. A3).

317 Due to the limited width (i.e., <10 μm) of the altered rim (i.e., secondary monazite) and the
318 chaotic patchy zoning of the partially altered core (i.e., mixture of pristine and secondary monazite),
319 the laser spot size (i.e., 10 μm) does not have the spatial resolution to resolve pristine and secondary
320 monazite. Nevertheless, despite the mixture sampling of pristine and secondary monazite, monazite
321 U–Pb data form a linear array and yield a lower intercept age of 158.6 ± 3.3 Ma (MSWD = 3.7). One
322 possible explanation is that the alteration of monazite occurred shortly after the precipitation of
323 pristine monazite, less than the error of the lower intercept age. Accordingly, these altered (or
324 partially altered) monazite domains with high common Pb could yield geologically reasonable lower
325 intercept ages, which overlap with the ages of pristine monazite within the margin of error. Similar
326 results have been reported from the Sri Lanka monazite (Seydoux-Guillaume et al. 2012) and the
327 Montasset monazite, France (Didier et al. 2013).

328 While monazite and xenotime do occur in contact with each other, monazite ages do not reflect the
329 *ca.* 135 Ma hydrothermal event recorded by xenotime rims formed through coupled dissolution-
330 reprecipitation reactions. One possible explanation is that this hydrothermal event only induced
331 partial dissolution of monazite, but no compositional alteration. This is supported by the fact that
332 monazite contains abundant unhealed micro-cracks with little to no evidence of compositional
333 change along their edges, and shows a more anhedral shape than xenotime.

334 **Compositional alteration of monazite and xenotime**

335 One feature of the studied monazite is Th enrichment in the altered monazite rims. This contrasts
336 with many natural monazite samples, which normally form secondary monazite with lower Th
337 concentrations (e.g., Poitrasson et al. 2000; Rasmussen and Muhling, 2007; 2009; Seydoux-

338 Guillaume et al. 2012) via dissolution-reprecipitation reactions at low temperatures (i.e., $\leq 400^\circ\text{C}$).
339 For these natural samples, that decreasing Th content may be attributed to the high Th content in
340 pristine monazite (i.e., >4 wt% ThO_2) and limited structural incorporation of Th in secondary
341 monazite at lower temperatures. This is because the substitution of huttonite (ThSiO_4) into monazite
342 lattice is temperature-dependent (Hetherington et al. 2010; Seydoux-Guillaume et al. 2012), with
343 higher structural incorporation of Th at higher temperatures and vice versa. Accordingly, monazite
344 alteration experiments conducted at high temperatures (i.e., $\geq 600^\circ\text{C}$) form secondary monazite with
345 high Th contents (Seydoux-Guillaume et al. 2002; Hetherington et al. 2010; Harlov et al. 2011),
346 while low-temperature alteration experiments (i.e., $\leq 600^\circ\text{C}$) result in secondary monazite with low
347 Th contents (e.g., Williams et al. 2011; Budzyń et al. 2015a; Grand'Homme et al. 2018).

348 In our case, Th enrichment in the altered monazite is likely due to the relative low Th
349 concentrations (<4.5 wt% ThO_2 , Tables A5, A7, A9). A low concentration of Th is typical for
350 hydrothermal monazite (Schandl and Gorton, 2004), which normally contains <4 wt% of ThO_2 (e.g.,
351 Schandl and Gorton, 2004, Catlos et al., 2013; Janots et al. 2012) and is frequently used to date
352 hydrothermal gold deposits (e.g., Rasmussen et al. 2006; Fielding et al. 2017; Zhao et al. 2019; Deng
353 et al. 2020; Liu et al. 2021). However, the mobility of Th during the alteration of hydrothermal
354 monazite has rarely been addressed, partially due to previous studies focused on isotopic dating and a
355 lack of careful examination to recognize potential alteration textures. This study demonstrates that
356 $^{208}\text{Pb}/^{232}\text{Th}$ ages, commonly overlooked in geochronological studies on hydrothermal monazite,
357 should be presented and discussed due to Th enrichment in the altered monazite.

358 In contrast to monazite, the mechanisms of xenotime alteration are less well-known and
359 understood due to its lower abundance in nature. Several works documented fluid-mediated

360 alteration of xenotime in nature. These studies demonstrate that xenotime may break down into
361 secondary phases such as apatite, epidote, and hingganite (Broska et al. 2005; Hetherington and
362 Harlov, 2008; Majka et al, 2011; Ondrejka et al. 2022). Xenotime could also undergo coupled
363 dissolution-precipitation reactions, resulting in compositional alterations that affected the age
364 record (e.g., Hetherington et al. 2008; Rasmussen et al. 2011; Fielding et al. 2017; Budzyń et al.
365 2018), but the fluids inducing the dissolution-precipitation reactions are not well characterized,
366 partially due to the lack of co-existing fluid inclusions. Experimental studies on xenotime alterations
367 focused on alkali-rich aqueous fluid conditions (e.g., Hetherington et al. 2010; Harlov and Wirth,
368 2012; Budzyń et al. 2015b, 2017; Budzyń and Sláma, 2019). Hetherington et al. (2010) reported
369 partial dissolution of xenotime in acid and brine fluids, but no compositional alteration. The recent
370 experimental work of Budzyń and Sláma (2019) confirms that xenotime may be affected by re-
371 equilibration induced by alkali-rich aqueous fluid via coupled dissolution-precipitation reactions
372 under temperature conditions of 550–650 °C, resulting in U–Pb age disturbance.

373 While it's widely accepted that CO₂ can promote the solubility of REE since CO₃²⁻ forms strong
374 complexes with the REE (e.g., Wood, 1990; Williams-Jones et al. 2000; Hetherington et al. 2010;
375 Zhou et al. 2016), the role of CO₂ in xenotime alterations has been rarely addressed. This study
376 presents an example of xenotime compositional alteration and resetting of U–Pb ages caused by
377 coupled dissolution-precipitation reactions, which are induced by low to moderate salinity
378 carbonic-aqueous fluids at low temperatures (i.e., <400°C). Since these fluids are commonly involved
379 in the formation of lode gold deposits (e.g., Groves et al. 1998; Goldfarb et al. 2005), it's crucial to
380 examine xenotime textures and recognize potential alteration textures before carrying out isotopic
381 dating of xenotime collected from these deposits.

382 **Two discrete gold mineralization events**

383 The *ca.* 135 Ma hydrothermal event (Fig. 10), recorded by the altered rim of xenotime with a
384 weighted mean $^{206}\text{Pb}/^{238}\text{U}$ age of 135.46 ± 0.93 Ma, is responsible for the deposition of native gold
385 and stage III tellurides (i.e., petzite, calaverite, altaite, tellurobismuthite) because these minerals
386 occur in contact with or as inclusions in xenotime rims (Figs. 4C–I). While abundant Early
387 Cretaceous ages (144–120 Ma, Fig. 10 and Table A10) have been reported from the Xiaoqinling gold
388 district, minerals directly in contact with gold have only been recently dated (i.e., a monazite U-Pb
389 age of 127.5 ± 0.7 and a rutile U-Pb age of 129.7 ± 4.3 Ma; Liu et al. 2021). The paragenetic
390 relationship between dated minerals and gold is unclear in many previous studies. For instance, dated
391 minerals in gold-bearing quartz veins or altered wall rocks do not necessarily result from the same
392 hydrothermal event responsible for gold deposition. This study presents robust textural and
393 geochronological evidence to justify a *ca.* 135 Ma gold mineralization event in the Xiaoqinling gold
394 district.

395 The *ca.* 157 Ma hydrothermal event, recorded by xenotime cores with a weighted mean $^{206}\text{Pb}/^{238}\text{U}$
396 age of 157.11 ± 0.83 Ma and monazite with a Tera-Wasserburg lower intercept age of 158.6 ± 3.3
397 Ma, is responsible for the earlier gold mineralization (i.e., lingbaoite-sylvanite-stützite/native
398 tellurium-sylvanite-stützite), since xenotime, monazite, and stage II tellurides were all observed as
399 primary inclusions in pyrite (Figs. 3, 4). The stage II tellurides, although they now appear much less
400 abundant than stage III tellurides and gold, are merely remnants of the stage II gold mineralization
401 (i.e., gold in the form of sylvanite ($[\text{Au,Ag}]_2\text{Te}_4$) after having been reworked by the later fluid event.
402 The early-stage gold mineralization could have played an important role in the later gold enrichment
403 process. For instance, recent studies (Jian et al. 2021, 2022b) reveal that stage II tellurides are

404 primary melt inclusions trapped as polymetallic droplets that scavenged gold from aqueous fluids
405 with high efficiency. During later hydrothermal events, polymetallic melt inclusions could be
406 released from the host mineral and continue to scavenge gold from fluids, due to fracturing of the
407 host mineral or migration of the melt inclusions to the crystal surface. Aside from S16 gold-bearing
408 quartz vein, the characteristic lingbaoite-sylvanite-bearing mineral assemblage, and by analogy, the
409 earlier gold mineralization event has also been observed in other parts of the Xiaoqinling gold
410 district, such as the S60 gold-bearing quartz vein (Jian et al. 2020, 2021, 2022b) and the Jinqu gold
411 deposit (Chang et al. 2020). Our study, therefore, reveals a previously overlooked yet important Late
412 Jurassic gold mineralization event in the Xiaoqinling gold district.

413 Late Jurassic ages have been only reported from the Luzhougou gold deposit (two Re-Os
414 molybdenite model ages of 149 ± 8.4 Ma and 154 ± 1.1 Ma; Li et al. 2012a) in the Xiaoqinling gold
415 district. The lack of reported Late Jurassic ages likely results from the scarcity of geochronometers
416 that are able to preserve the Late Jurassic age information after the Early Cretaceous hydrothermal
417 overprint. Most of the Early Cretaceous ages in the Xiaoqinling gold district were obtained from
418 $^{40}\text{Ar}/^{39}\text{Ar}$ dating of micas, with a few Re-Os molybdenite and U-Pb monazite ages (Fig. 10 and Table
419 A10). The low $^{40}\text{Ar}/^{39}\text{Ar}$ closure temperatures of micas (e.g., $\sim 300^\circ\text{C}$ for biotite and $\sim 400^\circ\text{C}$ for
420 muscovite; Harrison et al. 1985, 2009; Schaen et al. 2021), suggest their isotopic system could be
421 easily reset during later hydrothermal events. For instance, our study reveals that the *ca.* 135 Ma gold
422 mineralization event is characterized by the mineral assemblage of native gold-calaverite-petzite-
423 tellurobismuthite, which coexists with low to moderate salinity $\text{H}_2\text{O}-\text{CO}_2$ fluid inclusions along
424 healed fractures in quartz (Figs. 3I–K). The total homogenization temperatures of these fluid
425 inclusions cluster at 200 to 400°C , a range that overlaps with the $^{40}\text{Ar}/^{39}\text{Ar}$ closure temperatures of

426 biotite and muscovite.

427 To the east of the Xiaoqinling gold district, abundant Late Jurassic ages have been reported in the
428 adjacent Xiong'ershan region. Examples include the Wuzhangshan monzogranite pluton (SHRIMP
429 zircon U–Pb age of 157 ± 1 Ma: Mao et al. 2010), granitic porphyries in the Shangfanggou Mo
430 deposit (SHRIMP zircon U–Pb age of 158 ± 3 Ma, Mao et al. 2010), Nannihu Mo deposit (SHRIMP
431 zircon U–Pb age of 157 ± 3 Ma, Mao et al. 2010), Balipo Mo deposit (LA-ICP-MS zircon U–Pb age
432 of 155.9 ± 2.3 Ma, Jiao et al. 2009), Qiyugou Au deposit (SIMS zircon U–Pb ages of 157.3 ± 1.1 and
433 158.7 ± 1.2 Ma, Wang et al. 2020), a Mo (Au?) mineralized vein in the Huaixiangwa Au deposit (Re-
434 Os molybdenite mean age of 155.0 ± 2.2 Ma, Gao et al. 2018), and a Au mineralized vein in the
435 Luanling Au deposit (Re–Os molybdenite isochron age of 163 ± 2 Ma, Chao et al. 2019).
436 Accordingly, the large-scale Jurassic magmatism and associated mineralization event in eastern
437 China (e.g., Mao et al. 2021a, b; Goldfarb et al. 2021), in relation to the subduction of the paleo-
438 Pacific plate beneath the eastern China continent (Mao et al. 2021a), might have also caused
439 widespread gold mineralization in the Xiaoqinling gold district.

440

IMPLICATIONS

441 This study presents an example of xenotime compositional alteration and resetting of U–Pb ages
442 caused by coupled dissolution-precipitation reactions, which are induced by low to moderate
443 salinity carbonic-aqueous fluids at low temperatures. Gold minerals in contact with such composite
444 xenotime crystals could precipitate before, coeval with, or after the dated domains, depending on the
445 relation between the gold minerals and the dated xenotime domains. Since low to moderate salinity
446 carbonic-aqueous fluids are commonly involved in the formation of lode gold deposits, it's crucial to

21

447 examine xenotime textures and recognize potential alteration textures before carrying out isotopic
448 dating of xenotime collected from these deposits. Without prior compositional and textural
449 characterization, attempts to date such composite crystals could yield mixed age information and
450 meaningless ages.

451 This study also demonstrates that monazite and xenotime could be affected by low-temperature
452 hydrothermal alteration and yield discordant ages, resulting from incomplete replacement of mineral
453 domains or incorporation of common Pb. Common Pb could accumulate in the monazite and
454 xenotime along microcracks and grain boundaries. These features may be identified under high-
455 contrast SEM-BSE images but are not always visible in reflected-light photomicrographs or CL
456 images. During the alteration of hydrothermal monazite that typically contains low Th
457 concentrations, Th may be enriched in secondary monazite through coupled dissolution-
458 reprecipitation reactions. Accordingly, $^{208}\text{Pb}/^{232}\text{Th}$ ages, sometimes neglected in geochronological
459 studies on hydrothermal monazite from ore deposits, should be presented and discussed. This study
460 also highlights the potential of utilizing highly discordant U-Pb age data, which can be discarded in
461 geochronology studies but could potentially be used to constrain the age of metasomatic events as
462 the lower intercept in the Tera-Wasserburg Concordia diagrams.

463

ACKNOWLEDGMENTS

464 Bin Shi is thanked for his assistance with the SEM analysis. Lei Zhu and Huan Wang are thanked
465 for their assistance with the LA-ICP-MS analysis. Shuaiming Zhang and Guanguan Fang are thanked
466 for providing help and support during fieldwork. Constructive reviews by Sean Regan and an
467 anonymous reviewer considerably improved the paper and are greatly acknowledged. Callum

22

468 Hetherington is especially thanked for the editorial handling. This research was jointly funded by the
469 National Natural Science Foundation of China (41972093, 41672092) and the Fundamental Research
470 Funds for the Central Universities (2652020026).

471 **REFERENCES CITED**

472 Aleinikoff, J.N., Lund, K., and Fanning, C.M. (2015) SHRIMP U–Pb and REE data pertaining to the
473 origins of xenotime in Belt Supergroup rocks: evidence for ages of deposition, hydrothermal
474 alteration, and metamorphism: Canadian Journal of Earth Sciences, 52, 722–745.

475 Arne, D.C., Bierlein, F.P., Morgan, J.W., and Stein H.J. (2001) Re–Os dating of sulfides associated
476 with gold mineralization in central Victoria, Australia: Economic Geology, 96, 1455–1459.

477 Bateman, R., and Hagemann, S. (2004) Gold mineralisation throughout about 45 Ma of Archaean
478 orogenesis: Protracted flux of gold in the Golden Mile, Yilgarn craton, Western Australia:
479 Mineralium Deposita, 39, 536–559.

480 Bi, S.J., Li, J.W., and Li, Z.K. (2011) Geological significance and geochronology of Paleoproterozoic
481 mafic dykes of Xiaoqinling gold district, southern margin of the North China craton: Earth
482 Science—Journal of China University of Geosciences, 36, 17–32 (in Chinese with English
483 abstract).

484 Budzyń, B., Konečný, P., and Kozub-Budzyń, G.A. (2015a). Stability of monazite and disturbance of
485 the Th–U–Pb system under experimental conditions of 250–350° C and 200–400 MPa: Annales
486 Societatis Geologorum Poloniae, 85, 405–424.

487 Budzyń, B., and Kozub-Budzyń, G.A. (2015b). The stability of xenotime in high Ca and Ca–Na
488 systems, under experimental conditions of 250–350 C and 200–400 MPa: the implications for

- 489 fluid-mediated low-temperature processes in granitic rocks: *Geological Quarterly*, 59, 316–324.
- 490 Budzyń, B., Harlov, D.E., Kozub-Budzyń, G.A., and Majka, J. (2017). Experimental constraints on
491 the relative stabilities of the two systems monazite-(Ce)–allanite-(Ce)–fluorapatite and
492 xenotime-(Y)–(Y, HREE)-rich epidote–(Y, HREE)-rich fluorapatite, in high Ca and Na-Ca
493 environments under PT conditions of 200–1000 MPa and 450–750° C: *Mineralogy and
494 Petrology*, 111, 183–217.
- 495 Budzyń, B., Sláma, J., Kozub-Budzyń, G.A., Konečný, P., Holický, I., Rzepa, G., and Jastrzębski, M.
496 (2018) Constraints on the timing of multiple thermal events and re-equilibration recorded by
497 high-U zircon and xenotime: Case study of pegmatite from Piława Górna (Góry Sowie Block,
498 SW Poland): *Lithos*, 310–311, 65–85.
- 499 Budzyń, B., and Sláma, J. (2019) Partial resetting of U–Pb ages during experimental fluid-induced
500 re-equilibration of xenotime: *Lithos*, 346–347, 105163.
- 501 Budzyń, B., Wirth, R., Sláma, J., Birski, Ł., Tramm, F., Kozub-Budzyń, G.A., Rzepa, G., and
502 Schreiber, A. (2021). LA-ICPMS, TEM and Raman study of radiation damage, fluid-induced
503 alteration and disturbance of U-Pb and Th-Pb ages in experimentally metasomatised monazite:
504 *Chemical Geology*, 583, 120464.
- 505 Budzyń, B., Wirth, R., Sláma, J., Kozub-Budzyń, G.A., Rzepa, G., and Schreiber, A. (2022). A
506 detailed and comprehensive TEM, EPMA and Raman characterization of high-metamorphic
507 grade monazites and their U-Th-Pb systematics (the Góry Sowie Block, SW Poland): *Chemical
508 Geology*, 607, 121015.
- 509 Cai, N.Z, and Su, Z.B. (1985) Stratigraphic subdivision and distinction of primary rock-types of the
510 Taihua Group in the Xiaoqinling Mountain: *Regional Geology of China*, 13, 35–44 (in Chinese

- 511 with English abstract).
- 512 Catlos, E.J. (2013) Generalizations about monazite: Implications for geochronologic studies:
513 American Mineralogist, 98, 819–832.
- 514 Cao, J., Ye, H.S., Li, Z., Zhang, X.K., Wang, P., He, W. (2015) Geochronology, geochemistry and
515 petrogenesis of the Mogou alkalic pluton in the East Qinling orogenic belt: Acta Petrologica et
516 Mineralogica, 34, 665–684 (in Chinese with English abstract).
- 517 Chang, M., Liu, J.J., Carranza, E.J.M., Yin, C., Zhai, D.G., Wu, T., and Wang, D.Z. (2020) Gold-
518 telluride-sulfide association in the Jinqiu Au deposit, Xiaoqinling region, central China:
519 Implications for ore-forming conditions and processes: Ore Geology Reviews, 125, 103687.
- 520 Chao, W.W., Hayashi, K., Ye, H.S., Mao, J.W., Geng, Y.G., Bi, M.F., Wang, P., Pei, and Q.M. (2019)
521 Geology, mineralogy, geochronology, and sulfur isotope constraints on the genesis of the
522 Luanling gold telluride deposit, Western Henan province, central China: Resource Geology, 69,
523 333–350.
- 524 Cherniak, D.J., Watson, E.B., Grove, M. and Harrison, T.M. (2004) Pb diffusion in monazite: a
525 combined RBS/SIMS study: Geochimica et Cosmochimica Acta, 68, 829–840.
- 526 Cherniak, D.J. (2006) Pb and rare earth element diffusion in xenotime: Lithos, 88, 1–14.
- 527 Deng, J., and Wang, Q.F. (2016) Gold mineralization in China: Metallogenic provinces, deposit types
528 and tectonic framework: Gondwana Research, 36, 219–274.
- 529 Deng, J., Qiu, K.F., Wang, Q.F., Goldfarb, R., Yang, L.Q., Zi, J.W., Geng, J.Z., and Ma, Y. (2020) In
530 situ dating of hydrothermal monazite and implications for the geodynamic controls on ore
531 formation in the Jiaodong gold province, eastern China: Economic Geology, 115, 671–685.
- 532 Didier, A., Bosse, V., Boulvais, P., Bouloton, J., Paquette, J.L., Montel, J.M. and Devidal, J.L. (2013)

- 533 Disturbance versus preservation of U–Th–Pb ages in monazite during fluid–rock interaction:
534 textural, chemical and isotopic in situ study in microgranites (Velay Dome, France):
535 Contributions to Mineralogy and Petrology, 165, 1051–1072.
- 536 Dong, Y. and Santosh, M. (2016) Tectonic architecture and multiple orogeny of the Qinling Orogenic
537 Belt, Central China: Gondwana Research, 29, 1–40.
- 538 Dowling, K., and Morrison, G. (1989) Application of quartz textures to the classification of gold
539 deposits using North Queensland examples: Economic Geology Monograph 6, 342–355.
- 540 Du, Z.W., Ye, H.S., Mao, J.W., Fang, M., Cao, J., Wang, P., Wei, Z. and Ding, J.H. (2020)
541 Molybdenite Re–Os geochronology and isotope geochemical characteristics of Xigou
542 molybdenum deposit in Shaanxi Province and its geological significance: Mineral Deposits 39,
543 728–744 (in Chinese with English abstract).
- 544 Engi, M. (2017) Petrochronology based on REE–minerals: Monazite, allanite, xenotime: Reviews in
545 Mineralogy and Geochemistry, 83, 365–418.
- 546 Essarraj, S., Boiron, M.C., Cathelineau, M., and Fourcade, S. (2001) Multistage deformation of Au–
547 quartz veins (Laurieras, French Massif Central): Evidence for late gold introduction from
548 microstructural, isotopic and fluid inclusion studies: Tectonophysics, 336, 79–99.
- 549 Fan, H.R., Xie, Y.H., Zhai, M.G., and Jin, C.W. (2003) A three stage fluid flow model for
550 Xiaoqinling lode gold metallogenesis in the Henan and Shanxi provinces, central China: Acta
551 Petrologica Sinica, 19, 260–266 (in Chinese with English abstract).
- 552 Fielding, I.O.H., Johnson, S.P., Zi, J.W., Rasmussen, B., Muhling, J.R., Dunkley, D.J., Sheppard, S.,
553 Wingate, M.T.D., and Rogers, J.R. (2017) Using in situ SHRIMP U–Pb monazite and xenotime
554 geochronology to determine the age of orogenic gold mineralization: an example from the

- 555 Paulsens Mine, southern Pilbara Craton: *Economic Geology*, 112, 1205–1230.
- 556 Fougereuse, D, Micklethwaite, S, Ulrich, S, Miller, J, Godel, B, Adams, D.T., and McCuaig, T.C.
557 (2017) Evidence for two stages of mineralization in West Africa’s largest gold deposit: Obuasi,
558 Ghana: *Economic Geology*, 112, 3–22.
- 559 Fougereuse, D., Reddy, S.M., Saxey, D.W., Erickson, T.M., Kirkland, C.L., Rickard, W.D.A.,
560 Seydoux-Guillaume, A.M., Clark, C. and Buick, I.S. (2018) Nanoscale distribution of Pb in
561 monazite revealed by atom probe microscopy. *Chemical Geology*, 479, 251–258.
- 562 Gao, Y.L., Ye, H.S., Dai, F.Y., Niu, Y.J., Geng, Y.G., Chen, Z.G., and Li, Q. (2018) Geological
563 characteristics and ages of molybdenum and gold mineralization in the Huanxiangwa gold
564 deposit, Western Henan: *Geotectonica et Metallogenia*, 42, 191–304 (in Chinese with English
565 abstract).
- 566 Goldfarb, R.J., Baker, T., Dube, B., Groves, D.I., Hart, C.J., and Gosselin, P. (2005) Distribution,
567 character and genesis of gold deposits in metamorphic terranes: *Economic Geology* 100th
568 Anniversary Volume, p. 407–450.
- 569 Goldfarb, R.J., Mao, J.W., Qiu, K.F., and Goryachev, N. (2021) The great Yanshanian metallogenic
570 event of eastern Asia: Consequences from one hundred million years of plate margin
571 geodynamics: *Gondwana Research*, 100, 223–250.
- 572 Grand’Homme, A., Janots, E., Seydoux-Guillaume, A.M., Guillaume, D., Bosse, V., and Magnin, V.
573 (2016). Partial resetting of the U-Th-Pb systems in experimentally altered monazite: Nanoscale
574 evidence of incomplete replacement: *Geology*, 44, 431–434.
- 575 Grand'Homme, A., Janots, E., Seydoux-Guillaume, A. M., Guillaume, D., Magnin, V., Hövelmann,
576 J., Höschen, C., and Boiron, M.C. (2018). Mass transport and fractionation during monazite

- 577 alteration by anisotropic replacement. *Chemical Geology*, 484, 51–68.
- 578 Groves, D.I., Goldfarb, R.J., Gebre-Mariam, M., Hagemann, S.G., and Robert, F. (1998) Orogenic
579 gold deposits: A proposed classification in the context of their crustal distribution and
580 relationship to other gold deposit types: *Ore Geology Reviews*, 13, 7–27.
- 581 Harlov, D.E., Wirth, R., and Hetherington, C.J. (2011) Fluid-mediated partial alteration in monazite:
582 the role of coupled dissolution–reprecipitation in element redistribution and mass transfer:
583 *Contributions to Mineralogy and Petrology*, 162, 329–348.
- 584 Harlov, D.E., and Wirth, R. (2012) Experimental incorporation of Th into xenotime at middle to
585 lower crustal PT utilizing alkali-bearing fluids: *American Mineralogist*, 97, 641–652.
- 586 Harrison, T.M., Duncan, I., and McDougall, I. (1985) Diffusion of ^{40}Ar in biotite: Temperature,
587 pressure and compositional effects: *Geochimica et Cosmochimica Acta*, 49, 2461–2468.
- 588 Harrison, T.M., Célérier, J., Aikman, A.B., Hermann, J., and Heizler, M.T. (2009) Diffusion of ^{40}Ar
589 in muscovite: *Geochimica et Cosmochimica Acta*, 73, 1039–1051.
- 590 Hetherington, C.J., Jercinovic, M.J., Williams, M.L. and Mahan, K. (2008) Understanding geologic
591 processes with xenotime: Composition, chronology, and a protocol for electron probe
592 microanalysis: *Chemical Geology*, 254(3-4), 133–147.
- 593 Hetherington, C.J., and Harlov, D.E. (2008) Metasomatic thorite and uraninite inclusion in xenotime
594 and monazite from granitic pegmatites, Hydra anorthosite massif, southwestern Norway:
595 mechanics and fluid chemistry: *American Mineralogist*, 93, 806–820.
- 596 Hetherington, C.J., Harlov, D.E., and Budzyń, B. (2010) Experimental metasomatism of monazite
597 and xenotime: mineral stability, REE mobility and fluid composition: *Mineralogy and*
598 *Petrology*, 99, 165–184.

- 599 Janots, E., Berger, A., Gnos, E., Whitehouse, M., Lewin, E. and Pettke, T. (2012) Constraints on fluid
600 evolution during metamorphism from U–Th–Pb systematics in Alpine hydrothermal monazite:
601 Chemical Geology, 326, 61–71.
- 602 Jian, W., Lehmann, B., Mao, J.W., Ye, H.S., Li, Z.Y., He, H.J., Zhang, J.G., Zhang, H., and Feng,
603 J.W. (2015) Mineralogy, fluid characteristics, and Re-Os age of the Late Triassic Dahu Au-Mo
604 deposit, Xiaoqinling region, central China: Evidence for a magmatic-hydrothermal origin:
605 Economic Geology, 110, 119–145.
- 606 Jian, W., Mao, J.W., Lehmann, B., Li, Y.H., Ye, H.S., Cai, J.H., and Li, Z.Y. (2020) Lingbaoite,
607 AgTe₃, a new silver telluride from the Xiaoqinling gold district, central China: American
608 Mineralogist, 105, 745–755.
- 609 Jian, W., Mao, J.W., Lehmann, B., Cook, N.J., Xie, G.Q., Liu, P., Duan, C., Alles, J., and Niu, Z.J.
610 (2021) Au-Ag-Te-rich melt inclusions in hydrothermal gold-quartz veins, Xiaoqinling lode gold
611 district, central China: Economic Geology, 116, 1239–1248.
- 612 Jian, W, Mao, J.W., Lehmann, B., Chen, L., Song, S.W., Liu, J.C., Wang, P., and Rösel, D. (2022a)
613 Late Triassic Au-Mo mineralization in the Xiaoqinling region and a genetic connection to
614 carbonatitic magmatism: Ore Geology Reviews, 145, 104921.
- 615 Jian, W, Mao, J.W., Cook, N.J., Chen, L., Xu, J.D., Song, S.W., Hao, J.L., Li, R.Y., and Liu, J.C.
616 (2022b) Intracrystalline migration of polymetallic Au-rich melts in multistage hydrothermal
617 systems: example from the Xiaoqinling lode gold district, central China: Mineralium Deposita,
618 57, 147–154.
- 619 Jiao, J.G., Yuan, H.C., He, K., Sun, T., Xu, G., and Liu, R.P. (2009) Zircon U-Pb and molybdenite
620 Re-Os dating for the Balipo porphyry Mo deposit in East Qinling, China, and its geological

- 621 implication: *Acta Geologica Sinica*, 83, 1159–1166 (in Chinese with English abstract).
- 622 Liu, J.C., Wang, Y.T., Mao, J.W., Jian, W, Huang, S.K., Hu, Q.Q., Wei, R., and Hao, J.L. (2021)
- 623 Precise ages for lode gold mineralization in the Xiaozhiling gold field, southern margin of the
- 624 North China craton: new constraints from in situ U-Pb dating of hydrothermal monazite and
- 625 rutile: *Economic Geology*, 116, 773–786.
- 626 Li, J.W., Bi, S.J., Sebly, D., Chen, L., Vasconcelos, P., Thiede, D., Zhou, M.F., Zhao, X.F., Li, Z.K.,
- 627 and Qiu, H.N. (2012a) Giant Mesozoic gold provinces related to the destruction of the North
- 628 China craton: *Earth and Planetary Science Letters*, 349–350, 26–37.
- 629 Li, J.W., Li, Z.K., Zhou, M.F., Chen, L., Bi, S.J., Deng, X.D., Qiu, H.N., Cohen, B., Sebly, D., and
- 630 Zhao, X.F. (2012b) The Early Cretaceous Yangzhaiyu lode gold deposit, North China craton: A
- 631 link between craton reactivation and gold veining: *Economic Geology*, 107, 43–79.
- 632 Li, H.M., Chen, Y.C., Wang, D.H., Ye, H.S., Wang, Y.B., Zhang, C.Q., and Dai, J.Z. (2007) SHRIMP
- 633 U-Pb ages of metamorphic rocks and veins in the Xiaozhiling area, and their geological
- 634 significance: *Acta Petrologica Sinica*, 23, 2504–2512 (in Chinese with English abstract).
- 635 Li, S.M., Qu, L.Q., Su, Z.B., Huang, J.J., Wang, X.S., and Yue, Z.S. (1996) The geology and
- 636 metallogenic prediction of the gold deposit in Xiaozhiling: Beijing, Geological Publishing
- 637 House, 250 (in Chinese with English abstract).
- 638 Li, Y., Zhu, G., Su, N., Xiao, S., Zhang, S., Liu, C., Xie, C.L., Yin, H., and Wu, X. (2020). The
- 639 Xiaozhiling metamorphic core complex: A record of Early Cretaceous backarc extension along
- 640 the southern part of the North China Craton: *GSA Bulletin*, 132, 617–637.
- 641 Li, Z.Y., Ye, H.S., C, J., Zhang, X.K., and Zhai, L. (2014) Zircon U-Pb age, geochemistry and Sr-Nd-
- 642 Pb isotopic compositions of the granite porphyry in the Miaoling gold deposit of Songxian

- 643 County, Henan Province: *Acta Petrologica et Mineralogica*, 33, 424–440 (in Chinese with
644 English abstract).
- 645 Ma, Q., and Xu, Y.G. (2021) Magmatic perspective on subduction of Paleo-Pacific plate and
646 initiation of big mantle wedge in East Asia: *Earth-Science Reviews*, 213, 103473.
- 647 Majka, J., Pršek, J., Budzyń, B., Bačík, P., Barker, A. K., & Łodziński, M. (2011). Fluorapatite-
648 hingganite-(Y) coronas as products of fluid-induced xenotime-(Y) breakdown in the
649 Skoddefjellet pegmatite, Svalbard: *Mineralogical Magazine*, 75, 159–167.
- 650 Mao, J.W., Xie, G.Q., Zhang, Z.H., Li, X.F., Wang, Y.T., Zhang, C.Q., and Li, Y.F. (2005) Mesozoic
651 large scale metallogenic pulses in North China and corresponding geodynamic settings: *Acta*
652 *Geologica Sinica*, 21, 169–188 (in Chinese with English abstract).
- 653 Mao, J.W., Xie, G.Q., Pirajno, F., Ye, H.S., Wang, Y.B., Li, Y.F., Xiang, J.F., and Zhao, H.J. (2010)
654 Late Jurassic-Early Cretaceous granitoid magmatism in eastern Qinling, central-eastern China:
655 SHRIMP zircon U-Pb ages and tectonic implications: *Australian Journal of Earth Sciences*, 57,
656 51–78.
- 657 Mao, J.W., Zheng, W., Xie, G.Q., Lehmann, B., and Goldfarb, R. (2021a) Recognition of a Middle–
658 Late Jurassic arc-related porphyry copper belt along the southeast China coast: Geological
659 characteristics and metallogenic implications: *Geology*, 49, 592–596.
- 660 Mao, J.W., Liu, P., Goldfarb, R.J., Goryachev, N. A., Pirajno, F., Zheng, W., Zhou, M., Zhao, C., Xie,
661 G.Q., Yuan, S.D., and Liu, M. (2021b) Cretaceous large-scale metal accumulation triggered by
662 post-subductional large-scale extension, East Asia: *Ore Geology Reviews*, 136, 104270.
- 663 McNaughton, N. J., and Rasmussen, B. (2018) Geochemical characterisation of xenotime formation
664 environments using U-Th: *Chemical Geology*, 484, 109–189.

- 665 Ni, Z.Y., Wang, R.M., Tong, Y., Yang, C., and Dai, T.M. (2003) $^{207}\text{Pb}/^{206}\text{Pb}$ age of zircon and
666 $^{40}\text{Ar}/^{39}\text{Ar}$ of amphibole from plagioclase amphibolite in the Taihua Group, Luoning, Henan,
667 China: Geological Review, 49, 361–366 (in Chinese with English abstract).
- 668 Ondrejka, M., Molnárová, A., Putiš, M., Bačík, P., Uher, P., Voleková, B., Milovská, S, Mikuš, T. and
669 Pukančík, L. (2022) Hellandite-(Y)–hingganite-(Y)–fluorapatite retrograde coronae: a novel
670 type of fluid-induced dissolution–reprecipitation breakdown of xenotime-(Y) in the
671 metagranites of Fabova Hoľa, Western Carpathians, Slovakia: Mineralogical Magazine, 86,
672 586–605.
- 673 Parrish R.R. (1990) U–Pb dating of monazite and its application to geological problems: The
674 Canadian Journal of Earth Sciences, 27, 1431–1450.
- 675 Poitrasson, F., Chenery, S., and Shepherd, T.J. (2000) Electron microprobe and LA-ICP-MS study of
676 monazite hydrothermal alteration: Implications for U-Th-Pb geochronology and nuclear
677 ceramics: Geochimica et Cosmochimica Acta, 64, 3283–3297.
- 678 Putnis, A. (2002) Mineral replacement reactions: from macroscopic observations to microscopic
679 mechanisms: Mineralogical Magazine, 66, 689–708.
- 680 Putnis, A. (2009) Mineral replacement reactions: Reviews in Mineralogy and Geochemistry, 70, 87–
681 124.
- 682 Qiang, S.F. (2012) Mesozoic gold (Mo) mineralization in the northern melt, Xiaoqinling gold
683 district: evidence from the Qinnan and Qiaoshangzhai gold deposits: Unpublished PhD. Thesis,
684 Wuhan, China, China University of Geosciences, pp. 1–109 (in Chinese with English abstract).
- 685 Qiang, S.F., Bi, S.J., Deng, X.D., Guo, L.Q., and Li, J.W. (2013) Monazite U-Th-Pb ages of Qinnan
686 gold deposit, Xiaoqinling district: Implications for regional metallogenesis and tectonic setting:

- 687 Earth Science-Journal of China University of Geosciences, 38, 43–56 (in Chinese with English
688 abstract).
- 689 Rasmussen, B. (2005) Radiometric dating of sedimentary rocks: the application of diagenetic
690 xenotime geochronology: *Earth-Science Reviews*, 68, 197–243.
- 691 Rasmussen, B., Sheppard, S., and Fletcher, I. R. (2006) Testing ore deposit models using in situ U-Pb
692 geochronology of hydrothermal monazite: Paleoproterozoic gold mineralization in northern
693 Australia: *Geology*, 34, 77–80.
- 694 Rasmussen, B., and Muhling, J.R. (2007) Monazite begets monazite: Evidence for dissolution of
695 detrital monazite and reprecipitation of syntectonic monazite during low-grade regional
696 metamorphism: *Contributions to Mineralogy and Petrology*, 154, 675–689.
- 697 Rasmussen, B., and Muhling, J.R. (2009). Reactions destroying detrital monazite in greenschist-
698 facies sandstones from the Witwatersrand basin, South Africa: *Chemical Geology*, 264, 311–
699 327.
- 700 Rasmussen, B., Fletcher, I.R., and Muhling, J.R. (2011) Response of xenotime to prograde
701 metamorphism: *Contributions to Mineralogy and Petrology*, 162, 1259–1277.
- 702 Schaen, A.J., Jicha, B.R., Hodges, K.V., Vermeesch, P., Stelten, M.E., Mercer, C.M., Phillips, D.,
703 Rivera, T.A., Jourdan, F., Matchan, E.L. and Hemming, S.R. (2021) Interpreting and reporting
704 $^{40}\text{Ar}/^{39}\text{Ar}$ geochronologic data: *Geological Society of America Bulletin*, 133, 461–487.
- 705 Schandl, E.S., and Gorton, M.P. (2004) A textural and geochemical guide to the identification of
706 hydrothermal monazite: criteria for selection of samples for dating epigenetic hydrothermal ore
707 deposits: *Economic Geology*, 99, 1027–1035.
- 708 Schoene, B. (2014) U–Th–Pb geochronology. In: Holland, H.D., Turekian, K.K. (Eds.), *Treatise on*

- 709 Geochemistry (Second Edition), vol. 4.10. Elsevier, pp. 341–378.
- 710 Seydoux-Guillaume, A. M., Paquette, J. L., Wiedenbeck, M., Montel, J. M., and Heinrich, W. (2002)
- 711 Experimental resetting of the U–Th–Pb systems in monazite. *Chemical Geology*, 191, 165–181.
- 712 Seydoux-Guillaume, A.M., Goncalves, P., Wirth, R. and Deutsch, A. (2003) Transmission electron
- 713 microscope study of polyphase and discordant monazites: Site-specific specimen preparation
- 714 using the focused ion beam technique: *Geology*, 31, 973–976.
- 715 Seydoux-Guillaume, A.M., Montel, J.M., Bingen, B., Bosse, V., de Parseval, P., Paquette, J.L.,
- 716 Janots, E. and Wirth, R. (2012) Low-temperature alteration of monazite: Fluid mediated coupled
- 717 dissolution–precipitation, irradiation damage, and disturbance of the U–Pb and Th–Pb
- 718 chronometers: *Chemical Geology*, 330, 140–158.
- 719 Tang, L., Wagner, T., Fusswinkel, T., Zhang, S.T., Xu, B., Jia, L.H. and Hu, X.K. (2021) Magmatic-
- 720 hydrothermal evolution of an unusual Mo-rich carbonatite: a case study using LA-ICP-MS fluid
- 721 inclusion microanalysis and He–Ar isotopes from the Huangshui’an deposit, Qinling, China:
- 722 *Mineralium Deposita*, 56, 1133–1150.
- 723 Townsend, K.J., Miller, C.F., D’Andrea, J.L., Ayers, J.C., Harrison, T.M., and Coath, C.D. (2000)
- 724 Low temperature replacement of monazite in the Ireteba granite, southern Nevada:
- 725 Geochronological implications: *Chemical Geology*, 172, 95–112.
- 726 Wang, P., Mao, J.W., Ye, H.S., Jian, W., Chen, X.D., Tian, Y.F., He, S., Yan, J.M., Wu, S.K., and
- 727 Wan, L.M. (2020) The Qiyugou Au orefield — An intrusion-related gold system in the Eastern
- 728 Qinling ore belt, China: Constraints from SIMS zircon U-Pb, molybdenite Re-Os, sericite ⁴⁰Ar-
- 729 ³⁹Ar geochronology, in-situ S-Pb isotopes, and mineralogy: *Ore Geology Reviews*, 124,
- 730 1036362.

- 731 Wang, T.H., Mao, J.W., and Wang, Y.B. (2008) Research on SHRIMP U-Pb chronology in
732 Xiaoqinling-Xionger'shan area: The evidence of delamination of lithosphere in Qinling
733 orogenic belt: *Acta Petrologica Sinica*, 24, 1273–1287 (in Chinese with English abstract).
- 734 Wang, X.X., Wang, T., Jahn, B.M., Hu, N.G., and Chen, W. (2007) Tectonic significance of Late
735 Triassic post-collisional lamprophyre dykes from the Qinling Mountains (China): *Geological*
736 *Magazine*, 144, 837–848.
- 737 Wang, X.X., Wang, T., Castro, A., Pedreira, R., Lu, X.X., and Xiao, Q.H. (2011) Triassic granitoids
738 of the Qinling orogen, central China: Genetic relationship of enclaves and rapakivi-textured
739 rocks: *Lithos*, 126, 369–387.
- 740 Wang, Y.T., Mao, J.W., Lu, X.X., and Ye, A.W. (2002) $^{40}\text{Ar}/^{39}\text{Ar}$ dating and geological implication of
741 the auriferous altered rocks from the middle-deep section of the Q875 gold-quartz vein in the
742 Xiaoqinling area, Henan, China: *Chinese Science Bulletin*, 47, 1727–1738 (in Chinese with
743 English abstract).
- 744 Wang, Z.L., Gong, Q.J., Sun, X., Wu, F.F. and Wang, W.X. (2012) LA-ICP-MS zircon U-Pb
745 geochronology of quartz porphyry from the Niutougou gold deposit in Songxian county, Henan
746 province: *Acta Geologica Sinica*, 86, 370–382.
- 747 Williams-Jones, A.E., Samson, I.M., and Olivo, G.R. (2000) The genesis of hydrothermal fluorite-
748 REE deposits in the Gallinas Mountains, New Mexico: *Economic Geology*, 95, 327–341.
- 749 Williams, M.L., Jercinovic, M.J., Harlov, D.E., Budzyń, B., and Hetherington, C.J. (2011) Resetting
750 monazite ages during fluid-related alteration: *Chemical Geology*, 283, 218–225.
- 751 Wood, S.A. (1990) The aqueous geochemistry of the rare-earth elements and yttrium 2. Theoretical
752 predictions of speciation in hydrothermal solutions to 350°C at saturation vapor pressure:

- 753 Chemical Geology, 88, 99–125
- 754 Wu, F.Y., Yang, J.H., Xu, Y.G., Wilde, S.A., and Walker, R.J. (2019) Destruction of the North China
755 Craton in the Mesozoic: Annual Review of Earth and Planetary Sciences, 47, 173–195.
- 756 Wu, S., Wörner, G., Jochum, K.P., Stoll, B., Simon, K., and Kronz, A. (2019) The preparation and
757 preliminary characterisation of three synthetic andesite reference glass materials (ARM-1,
758 ARM-2, ARM-3) for in situ microanalysis: Geostandards and Geoanalytical Research, 43, 567–
759 584.
- 760 Wu, S., Yang, M., Yang, Y.H., Xie, L.W., Huang, C., Wang, H., and Yang, J.H. (2020) Improved in
761 situ zircon U–Pb dating at high spatial resolution (5–16 μm) by laser ablation–single collector–
762 sector field–ICP–MS using Jet sample and X skimmer cones: International Journal of Mass
763 Spectrometry, 456, 116394.
- 764 Wu, S., Yang, Y., Jochum, K.P., Romer, R.L., Glodny, J., Savov, I.P., Agostini, S., De Hoog, J.C.M.,
765 Peters, S.T.M., Kronz, A., Zhang, C., Bao, Z., Wang, X., Li, Y., Tang, G., Feng, L., Yu, H., Li,
766 Z., Le, Z., Lin, J., Zeng, Y., Xu, C., Wang, Y., Cui, Z., Deng, L., Xiao, J., Liu, Y., Xue, D., Di,
767 Z., Jia, L., Wang, H., Xu, L., Huang, C., Xie, L., Pack, A., Wörner, G., He, M., Li, C., Yuan, H.,
768 Huang, F., Li, Q., Yang, J., Li, X., and Wu, F. (2021) Isotopic compositions (Li–B–Si–O–Mg–Sr–
769 Nd–Hf–Pb) and $\text{Fe}^{2+}/\Sigma\text{Fe}$ ratios of three synthetic andesite glass reference materials (ARM-1,
770 ARM-2, ARM-3): Geostandards and Geoanalytical Research, 45, 719–745.
- 771 Xiong, S.F., Ding, Z.J., Yao, S.Z., Xiong, J., Hu, X.L., He, M.C., and Tan, M.T. (2013)
772 Characteristics of ore-forming fluid of Yangzhaiyu gold deposit in Xiaoqinling gold district,
773 Henan Province: Mineral Deposits, 32, 1249–1261 (in Chinese with English abstract).
- 774 Xu, C., Kynicky, J., Chakhmouradian, A.R., Qi, L., and Song, W. (2010) A unique Mo deposit

- 775 associated with carbonatites in the Qinling orogenic belt, central China: *Lithos* 118, 50–60.
- 776 Xu, Q.D., Zhong, Z.Q., Zhou, H.W., Yang, F.C., and Tang, X.C. (1998) $^{40}\text{Ar}/^{39}\text{Ar}$ dating of the
777 Xiaoqinling Area in Henan Province: *Geological Review*, 44, 323–327 (in Chinese with English
778 abstract).
- 779 Zhao, S.R., Li, J.W., Lentz, D., Bi, S.J., Zhao, X.F., and Tang, K.F. (2019) Discrete mineralization
780 events at the Hongtuling Au-(Mo) vein deposit in the Xiaoqinling district, southern North China
781 Craton: evidence from monazite U-Pb and molybdenite Re-Os dating: *Ore Geology Reviews*,
782 109, 413–425.
- 783 Zheng, H., Chen, H.Y., Li, D.F., Wu, C., Chen, X. and Lai, C.K. (2020) Timing of carbonatite hosted
784 U-polymetallic mineralization in the supergiant Huayangchuan deposit, Qinling Orogen:
785 constraints from the titanite U-Pb and molybdenite Re-Os dating: *Geoscience Frontiers*, 11,
786 1581–1592.
- 787 Zhou, H.W., Zhong, Z.Q., Ling, W.L., Zhong, G.L., and Xu, Q.D. (1998) Sm-Nd isochron for the
788 amphibolites within Taihua complex from Xiao Qinling area, Western Henan and its geological
789 implications: *Geochimica*, 27, 367–372 (in Chinese with English abstract).
- 790 Zhou, L., Mavrogenes, J., Spandler, C. and Li, H. (2016) A synthetic fluid inclusion study of the
791 solubility of monazite-(La) and xenotime-(Y) in H₂O-Na-K-Cl-F-CO₂ fluids at 800° C and 0.5
792 GPa: *Chemical Geology*, 442, 121–129.

793

FIGURE CAPTIONS

- 794 Fig. 1. Geologic map of the Xiaoqinling gold district and its position in China (compiled from Jian et
795 al. 2015, 2021; Liu et al. 2021).

796

797 Fig. 2. Typical features of the S16 gold-bearing quartz vein shown by photographs. A. B.
798 Underground exposure. C. Hand specimen. D. Polished thick section showing the occurrences of
799 pyrite (euhedral large crystals), telurides (black cloudy aggregates), and xenotime (very fine-grained
800 red cloudy aggregates).

801

802 Fig. 3. Two stages of gold mineralization shown by photomicrographs (A–I: plane-polarized
803 reflected light, J: reflected-transmitted light image created through focus stacking, K: reflected-
804 transmitted light). A–H. Distribution of two stages (II, III) of minerals within and near two pyrite
805 grains. I. Native gold and telurides (stage III) occur as inclusions along a healed microfracture in
806 quartz. J–K. Native gold and teluride (stage III) coexist with low to moderate salinity H₂O-CO₂ fluid
807 inclusions along healed microfractures in quartz. Abbreviations: Alt = altaite, Au = gold, Bn =
808 bornite, Clv = calaverite, Ccp = chalcopyrite, Gn = galena, Lb = lingbaoite, Ptz = petzite, Py =
809 pyrite, Qz = quartz, Stz = stützite, Syv = sylvanite, Tbi = tellurobismuthite, Te = native tellurium.

810

811 Fig. 4. Occurrence of xenotime and monazite shown by photomicrographs (D, F, H: plane-polarized
812 reflected light), BSE images (A–C, E, G), and CL image (I). A–C. Xenotime and monazite occur as
813 inclusions in pyrite. D–G. Native gold and telurides (stage III) occur in contact with xenotime. The
814 two xenotime grains were dated by LA-ICP-MS. Their CL images with analyzed spots and ages
815 labeled are shown in Fig.5. G. Xenotime rims are brighter than core zones in BSE images. H–I.
816 Native gold and telurides (stage III) occur in contact with the rim of a xenotime grain or as
817 inclusions in the altered domains of the xenotime. Note that altered domains of xenotime are brighter

38

818 in CL image, while the unaltered domains are darker and show oscillatory zoning. Abbreviations: Alt
819 = altaite, Au = gold, Clv = calaverite, Mnz = monazite, Ptz = petzite, Py = pyrite, Qz = quartz, Xtm =
820 xenotime.

821

822 Fig. 5. Cathodoluminescence images of xenotime grains after LA-ICP-MS analysis. The 10 μm and
823 16 μm laser pits are for U-Th-Pb isotope and trace element analysis, respectively. SEM-BSE images
824 of the 10 xenotime grains before LA-ICP-MS analysis are shown in Figure A1. WDS X-ray maps (Y,
825 U, Th, Pb) of 6 xenotime grains before LA-ICP-MS analysis are shown in Figure A2.

826

827 Fig. 6. SEM-BSE images of monazite grains after LA-ICP-MS analysis. $^{206}\text{Pb}/^{238}\text{U}$, $^{207}\text{Pb}/^{235}\text{U}$ and
828 $^{208}\text{Pb}/^{232}\text{Th}$ ages of the analyzed spots are indicated.

829

830 Fig. 7. REE patterns of the xenotime and monazite. The data are normalized to C1 chondrite
831 composition as compiled in Sun and McDonough (1989).

832

833 Fig. 8. Tera-Wasserburg Concordia diagrams and weighted mean age diagrams for xenotime and
834 monazite.

835

836 Fig. 9. Two episodes of gold mineralization and growth of monazite and xenotime illustrated by
837 schematic drawing.

838

839 Fig. 10. Age distribution of gold deposits from the Xiaoqinling gold district. The age data, detailed in
840 the Appendix (Table A10), were compiled from Xu et al. (1998), Wang et al. (2002), Li et al. (2012a,
841 b), Qiang, 2012, Qiang et al. 2013, Zhao et al. (2019), and Liu et al. (2021).

842

843

APPENDIX

844 Fig. A1. SEM-BSE images of the 10 xenotime grains before LA-ICP-MS analysis.

845

846 Fig. A2. WDS X-ray maps of 6 xenotime grains before LA-ICP-MS analysis.

847

848 Fig. A3. Characterizations of the largest monazite grain before LA-ICP-MS analysis shown by BSE
849 image (A), photomicrographs (B: plane-polarized reflected light; C: plane-polarized reflected light
850 with gamma enhancement), and WDS X-ray maps (D–H).

851

852 Table A1. Analytical conditions of EPMA measurements of xenotime and monazite

853

854 Table A2. Analytical conditions of LA-ICP-MS U-Th-Pb analysis of xenotime and monazite

855

856 Table A3. Analytical conditions of LA-ICP-MS trace element analysis of xenotime

857

858 Table A4. Analytical conditions of LA-ICP-MS trace element analysis of monazite

859

- 860 Table A5. Electron microprobe data of xenotime and monazite
- 861
- 862 Table A6. LA-ICP-MS trace element data of xenotime
- 863
- 864 Table A7. LA-ICP-MS trace element data of monazite
- 865
- 866 Table A8. LA-ICP-MS U-Th-Pb data of xenotime
- 867
- 868 Table A9. LA-ICP-MS U-Th-Pb data of monazite
- 869
- 870 Table A10. Age data of gold deposits from the Xiaoqinling gold district
- 871

Fig. 1

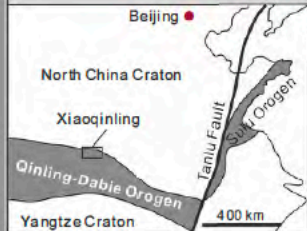
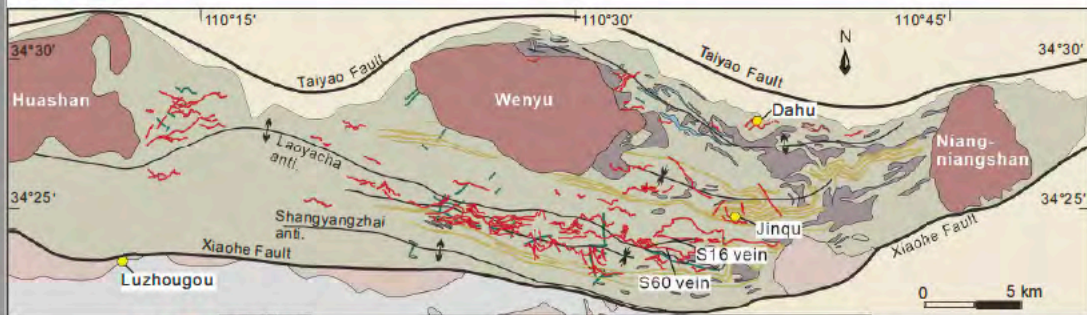


Fig. 2

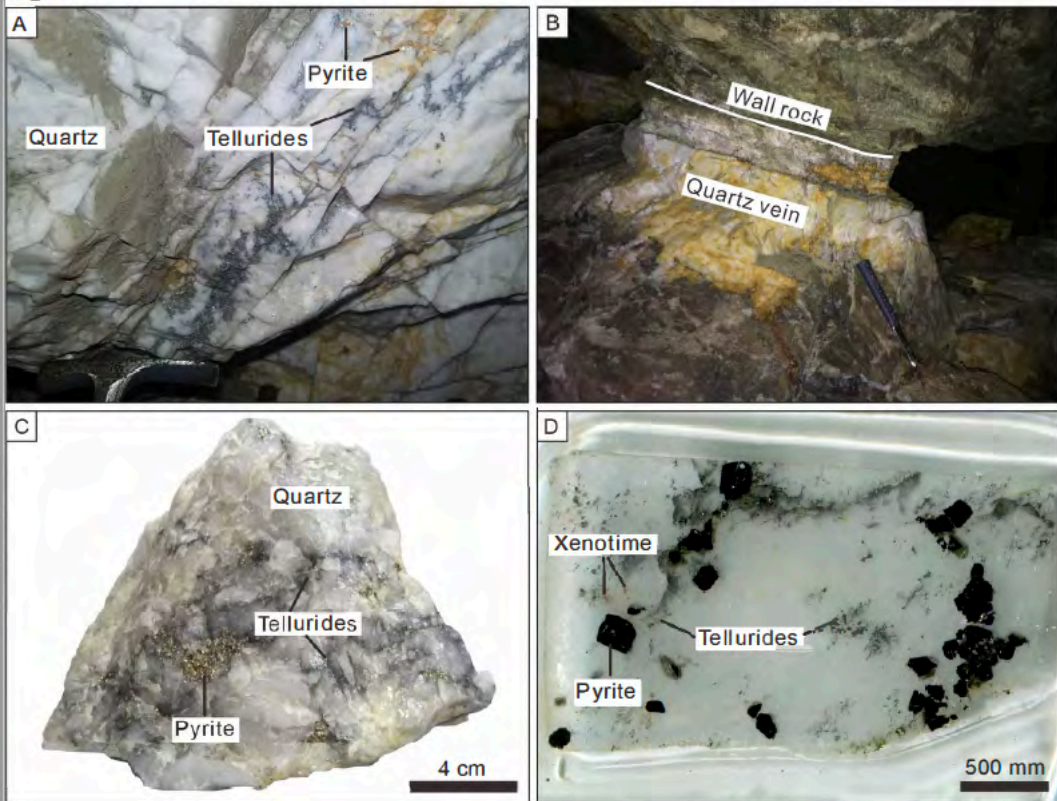


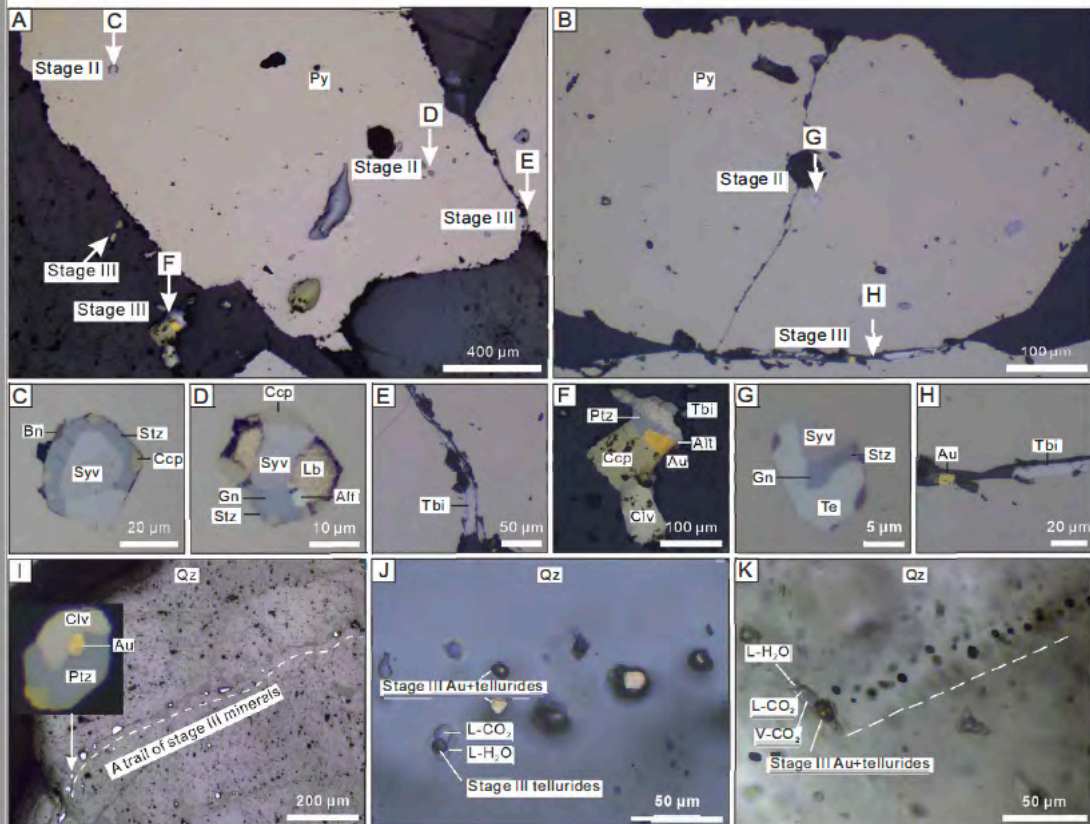
Fig. 3

Fig. 4

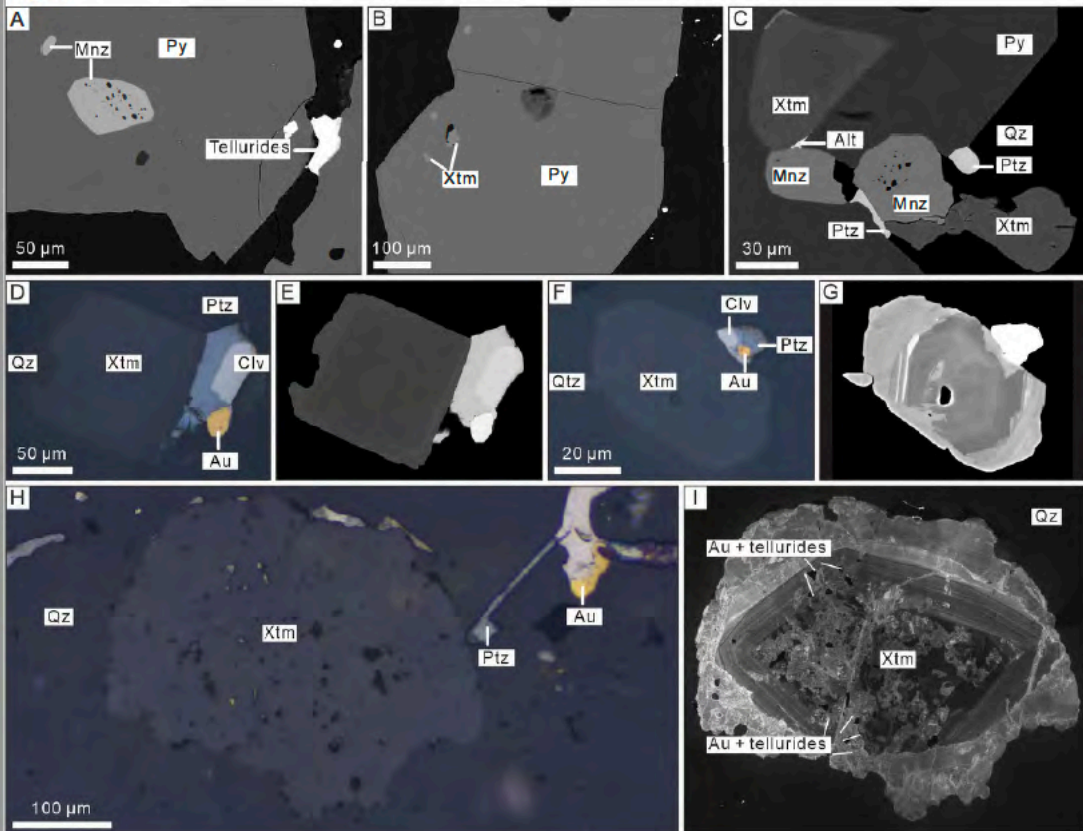


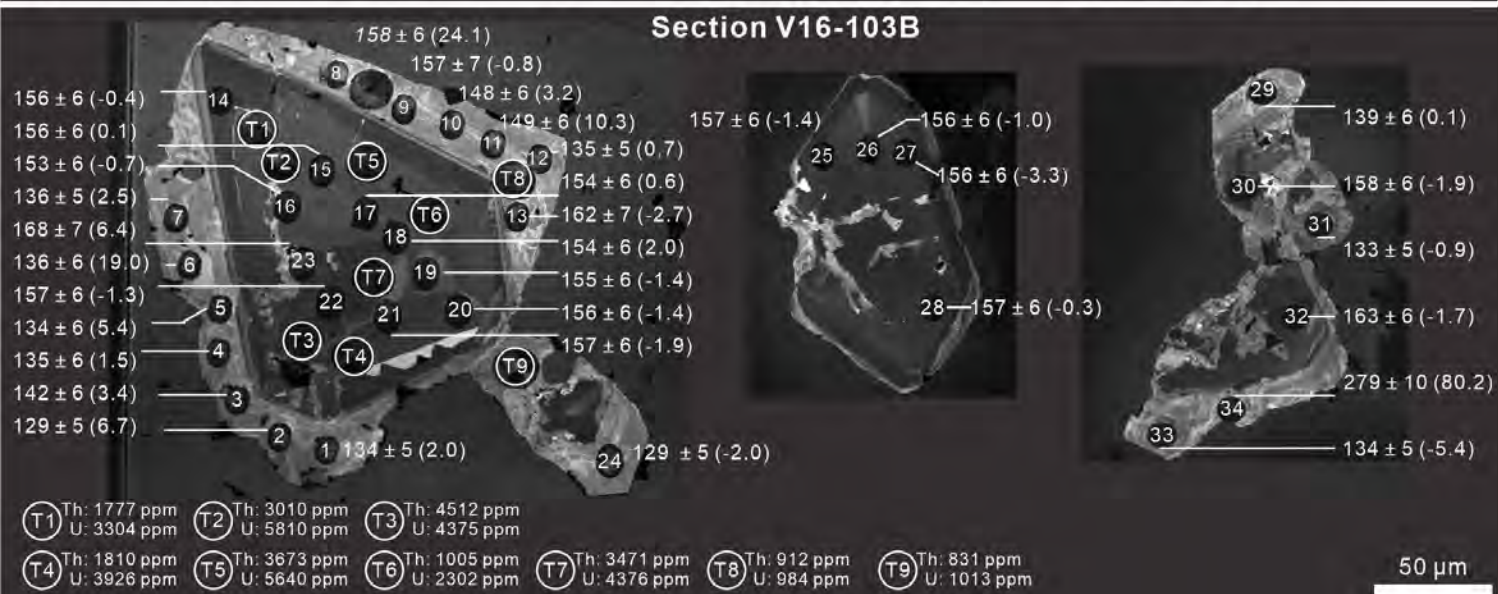
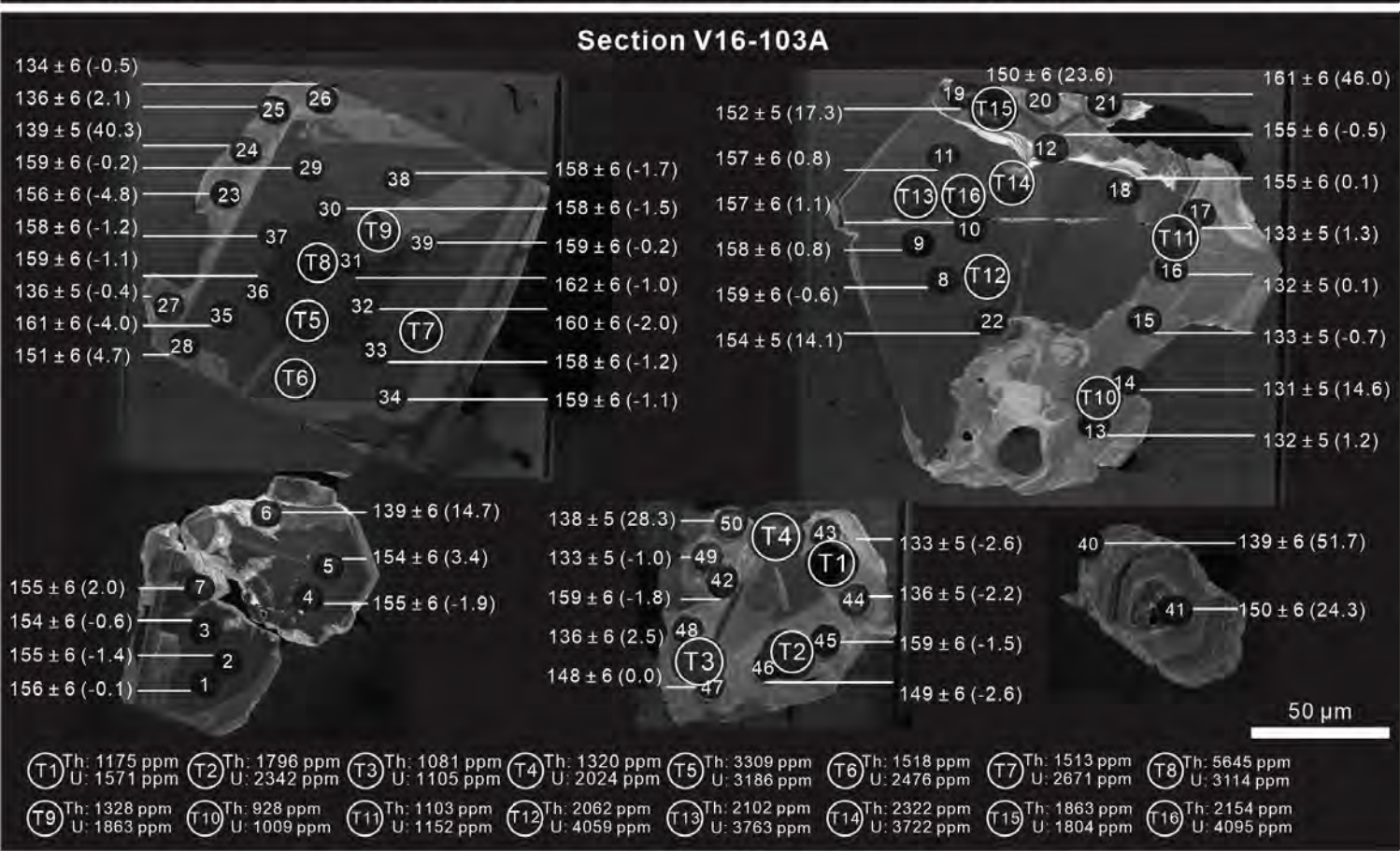
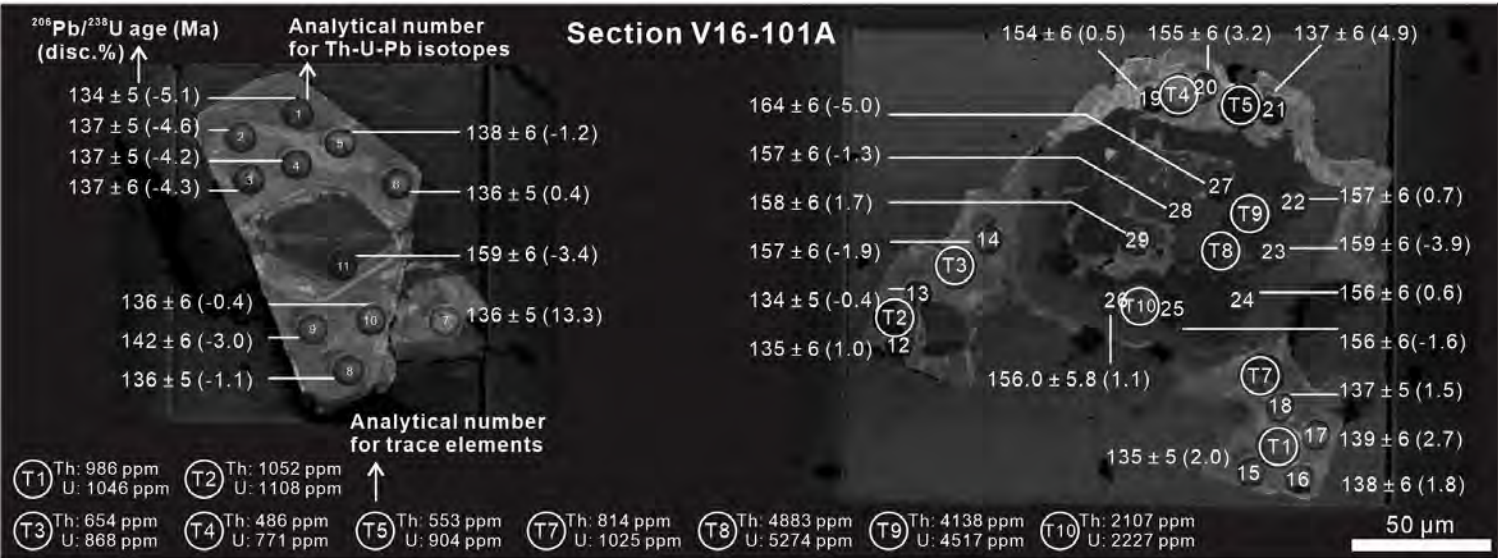
Fig. 5

Fig. 6

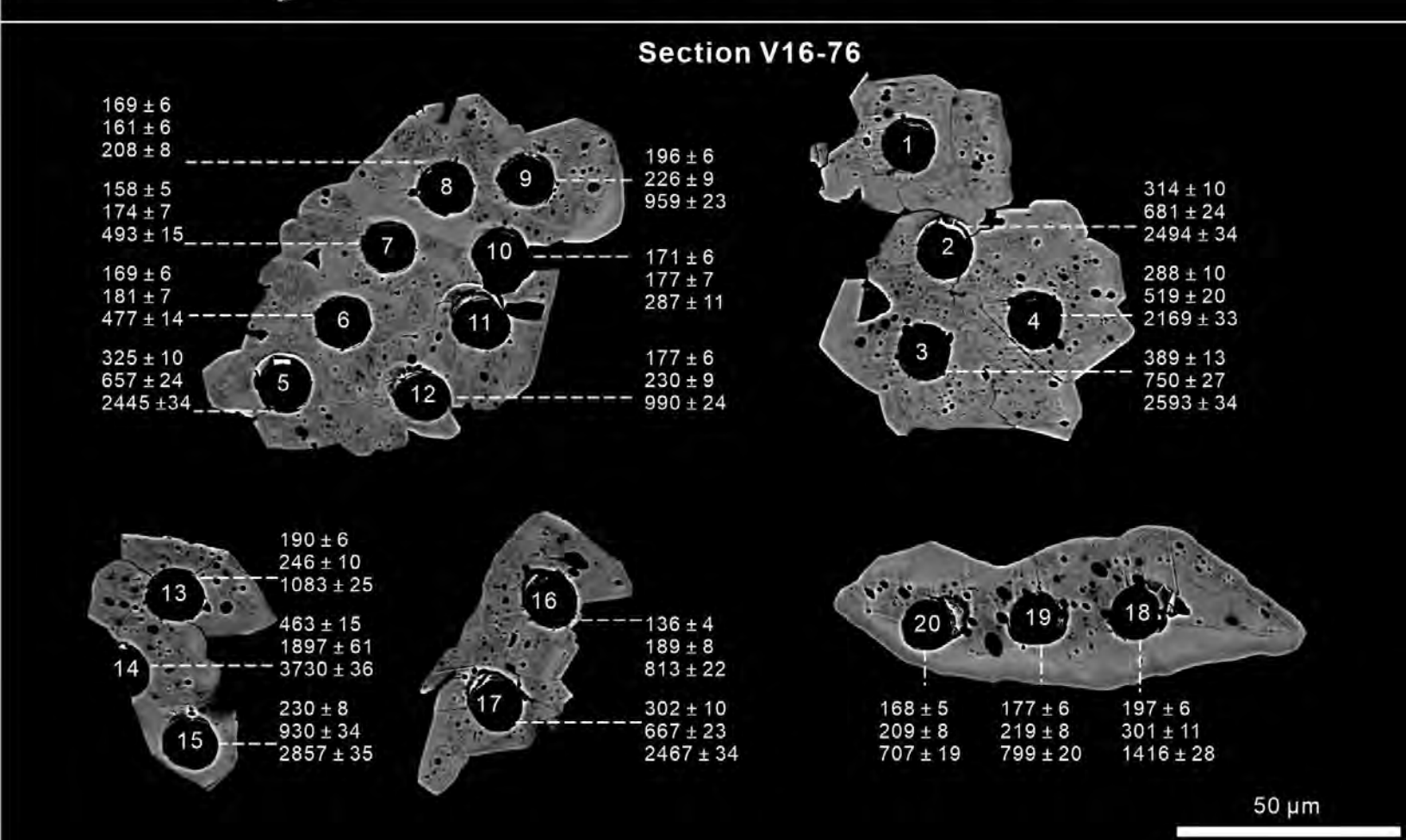
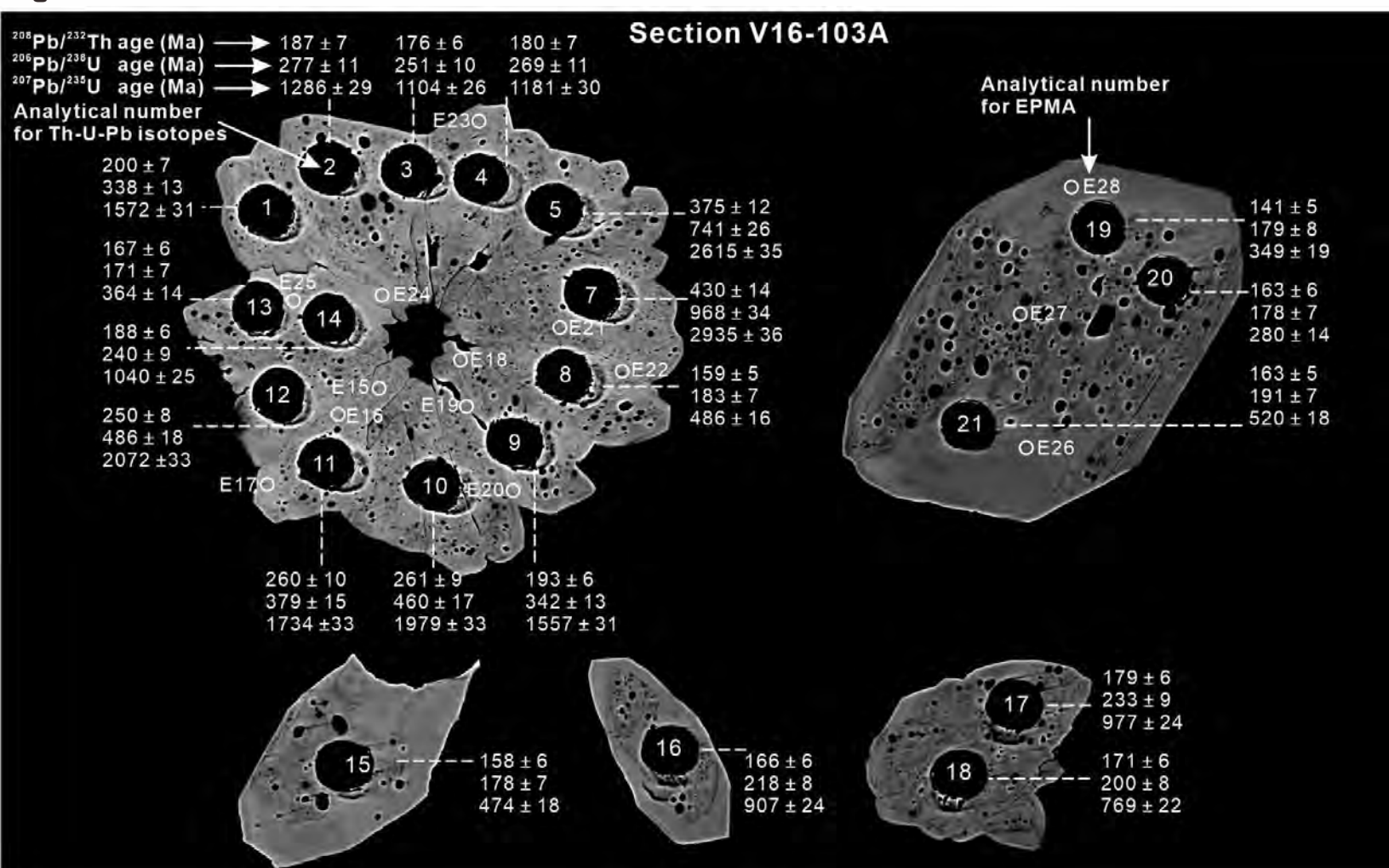


Fig. 7

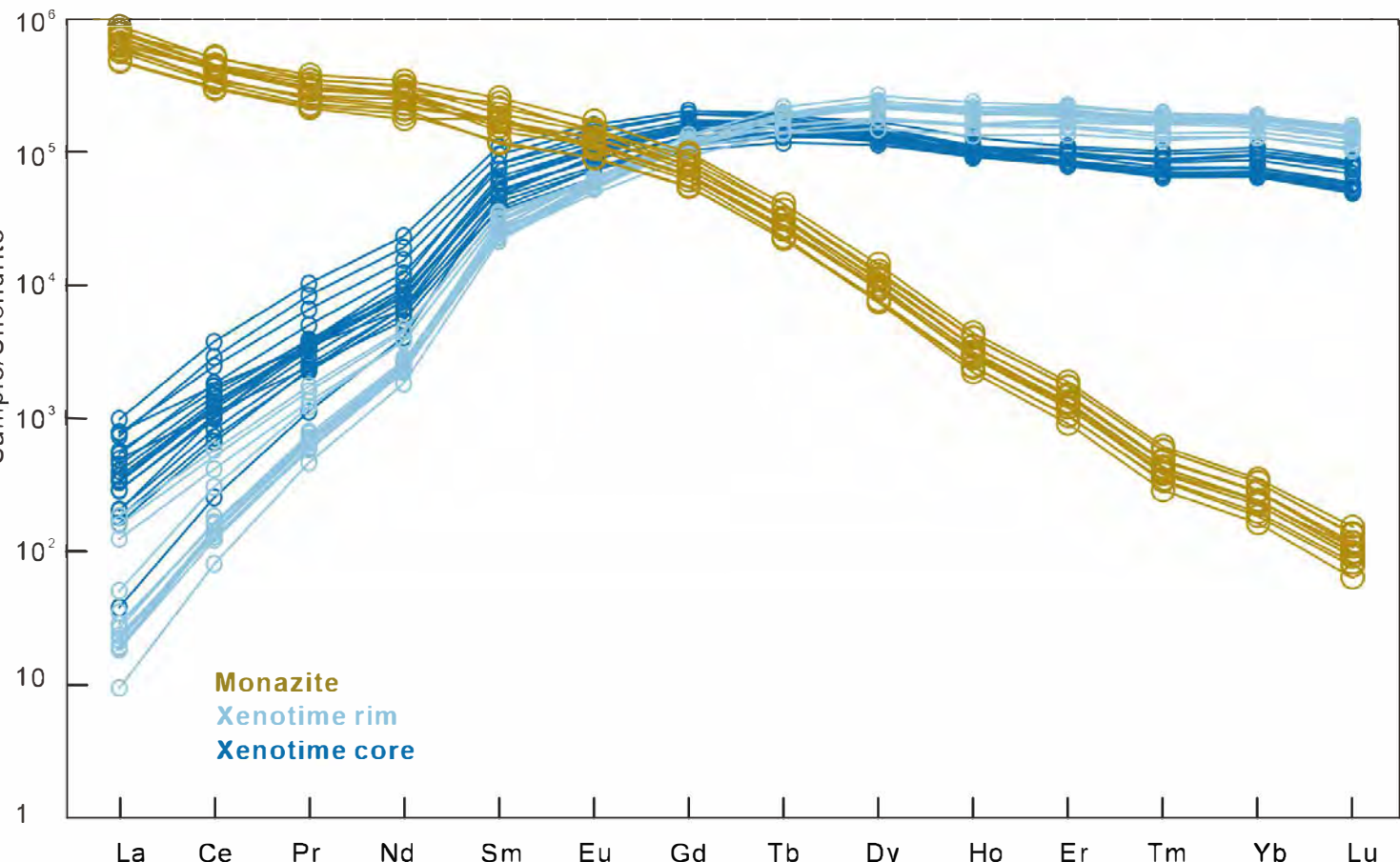


Fig. 8

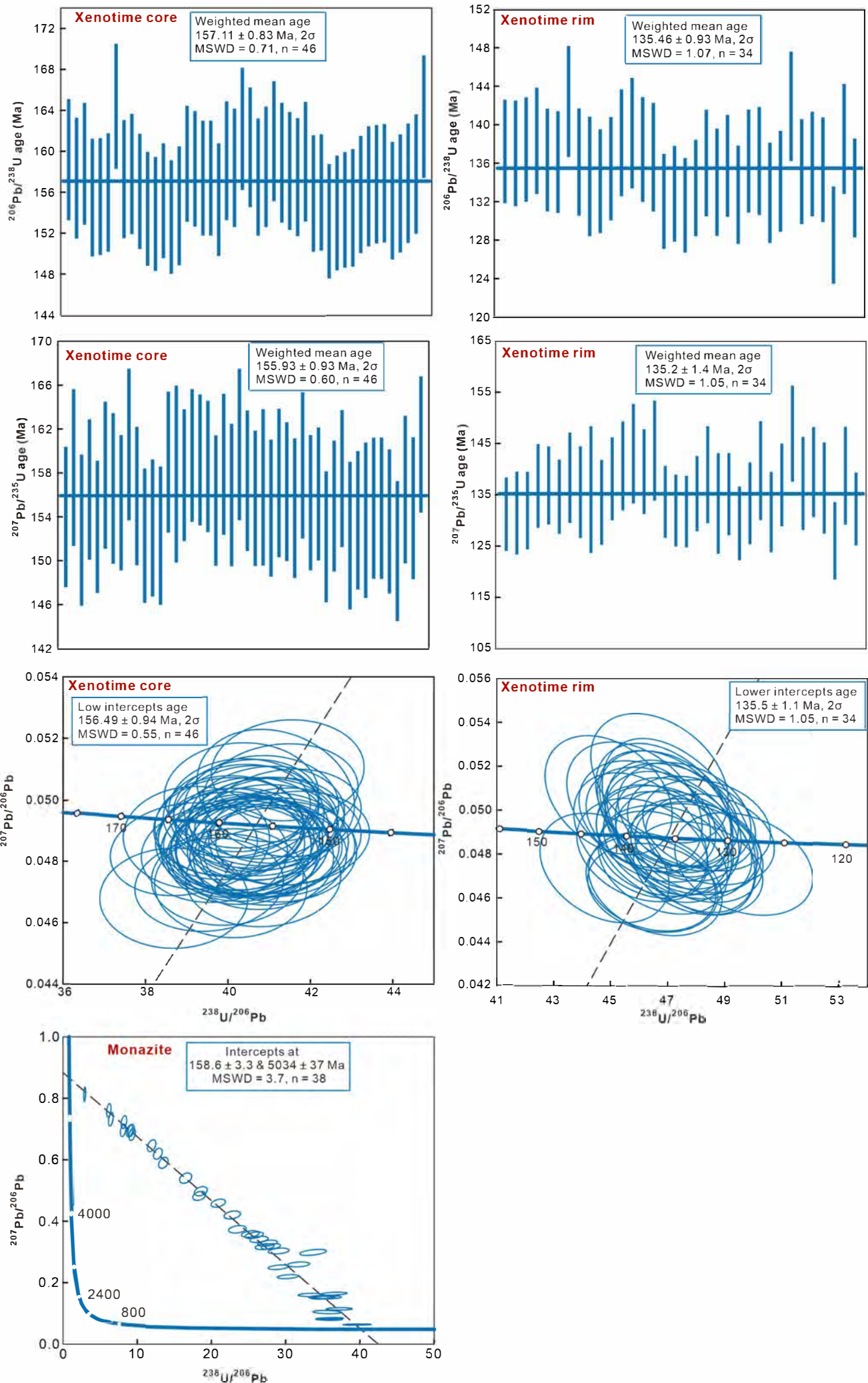
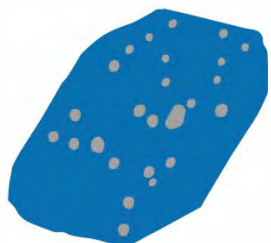


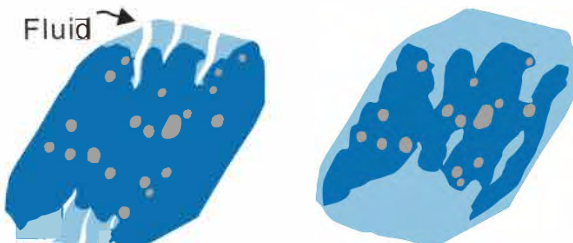
Fig. 9

ca. 157 Ma

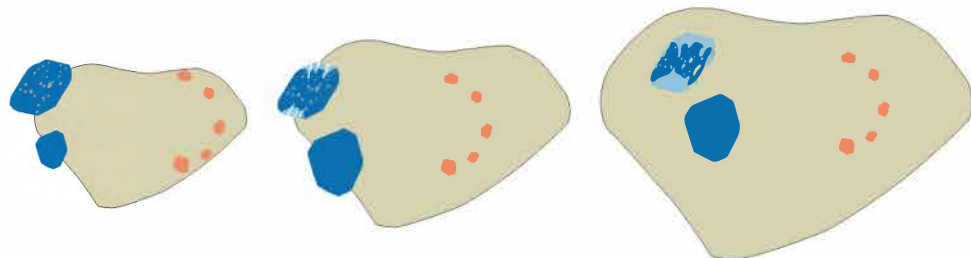
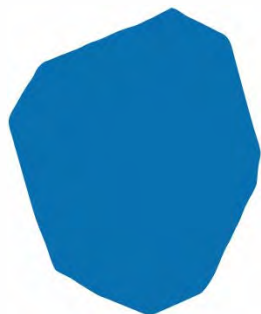
Growth of pristine monazite



Dissolution–reprecipitation of monazite

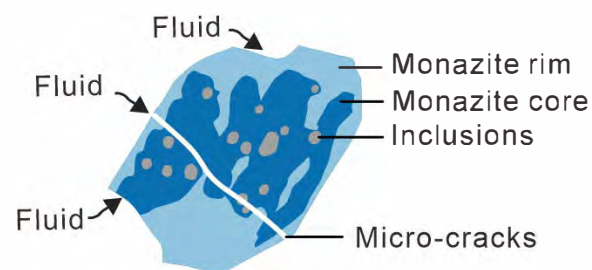


Growth of pristine xenotime



ca. 135 Ma

Dissolution of monazite



Dissolution–reprecipitation of xenotime

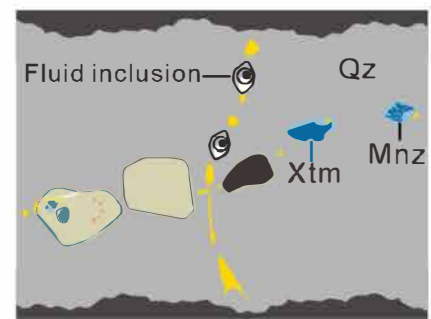
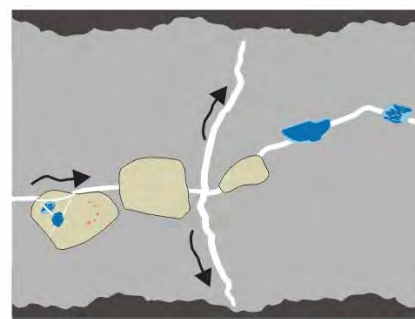
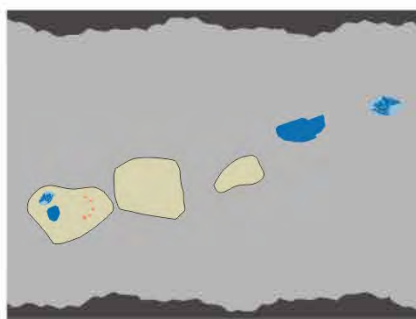
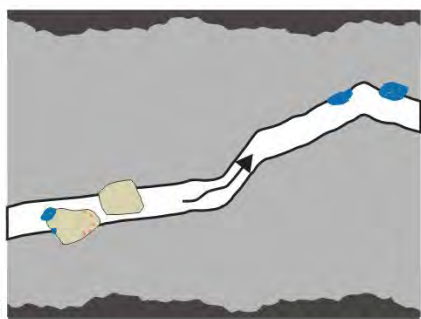
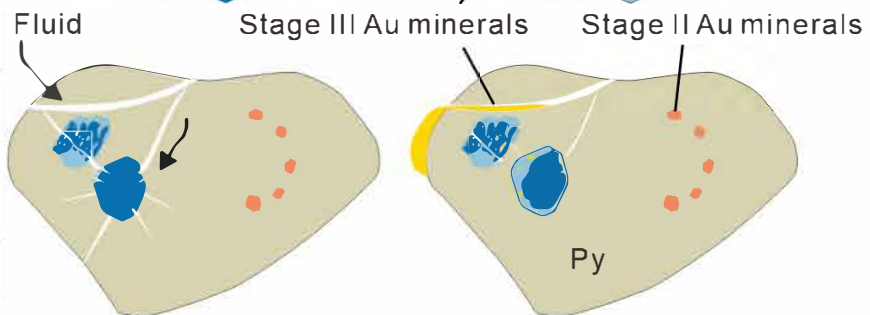
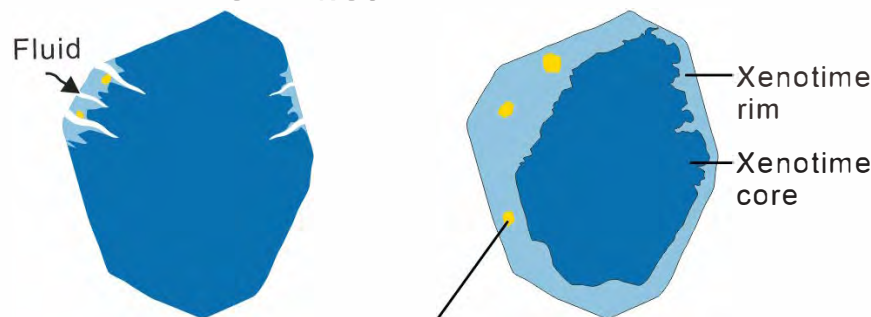


Fig. 10

